Physics of Fluids

Topology of the second-order constitutive model based on the Boltzmann–Curtiss kinetic equation for diatomic and polyatomic gases

Cite as: Phys. Fluids **32**, 026104 (2020); https://doi.org/10.1063/1.5133079
Submitted: 22 October 2019 . Accepted: 04 February 2020 . Published Online: 25 February 2020

S. Singh, A. Karchani, K. Sharma, and R. S. Myong (명노신)

Physics of Fluids ARTICLE scitation.org/journal/phf

Topology of the second-order constitutive model based on the Boltzmann–Curtiss kinetic equation for diatomic and polyatomic gases

Cite as: Phys. Fluids 32, 026104 (2020); doi: 10.1063/1.5133079
Submitted: 22 October 2019 • Accepted: 4 February 2020 •
Published Online: 25 February 2020

S. Singh,[1] A. Karchani,[2,a)] K. Sharma,[3] and R. S. Myong (명노신)[3,b)]

AFFILIATIONS

[1]School of Physical and Mathematical Sciences, Nanyang Technological University, 21 Nanyang Link 637371, Singapore
[2]ANSYS Inc., Lebanon, New Hampshire 03766, USA
[3]School of Mechanical and Aerospace Engineering and ACTRC, Gyeongsang National University, Jinju, Gyeongnam 52828, South Korea

[a)]Formerly research assistant at School of Mechanical and Aerospace Engineering, Gyeongsang National University, Jinju, South Korea.
[b)]**Author to whom correspondence should be addressed:** myong@gnu.ac.kr. **Tel.:** +82-55-772-1645

ABSTRACT

The topological aspects of fluid flows have long been fascinating subjects in the study of the physics of fluids. In this study, the topology of the second-order Boltzmann–Curtiss constitutive model beyond the conventional Navier–Stokes–Fourier equations and Stokes's hypothesis was investigated. In the case of velocity shear, the topology of the second-order constitutive model was shown to be governed by a simple algebraic form. The bulk viscosity ratio in diatomic and polyatomic gases was found to play an essential role in determining the type of topology: from an ellipse to a circle, to a parabola, and then finally to a hyperbola. The topology identified in the model has also been echoed in other branches of science, notably in the orbits of planets and comets and Dirac cones found in electronic band structures of two-dimensional materials. The ultimate origin of the existence of the topology was traced to the coupling of viscous stress and velocity gradient and its subtle interplay with the bulk viscosity ratio. In the case of compression and expansion, the topology of the second-order constitutive model was also found to be governed by a hyperbola. The trajectories of solutions of two representative flow problems—a force-driven Poiseuille gas flow and the inner structure of shock waves—were then plotted on the topology of the constitutive model, demonstrating the indispensable role of the topology of the constitutive model in fluid dynamics.

I. INTRODUCTION

Topology is concerned with the properties of objects (or systems) that are preserved under continuous deformations (or changes). It appears in almost every branch of physics and mathematics including algebra, analysis, geometry, mathematical modeling, discrete mathematics, industrial mathematics, and mathematical fluid dynamics. In particular, the study of the topological aspects of the dynamics of fluids and plasmas has been very instructive for describing fluid flows with complicated physics.[1] The spatial topological representation of fluid flows begins with the study of curves, surfaces, and other objects in two- and three-dimensional space, which divides the flow into separate regions. One of the central ideas in topology is that objects can be treated in their own right, and knowledge of objects is independent of how they are embedded in spatial or phase space.

The topological ideas in fluid dynamics originated with the renowned works by Helmholtz[2] and Kelvin[3] on vortex dynamics. Topological ideas were also investigated in the work of Arnold[4] on the Euler equation for an ideal fluid on a group of volume-preserving diffeomorphism. Later, these topological ideas were applied to various aspects of the dynamics of fluids and plasmas such as vorticity structure,[5] interfacial flow,[6] stability of

magneto-hydrodynamic shock waves,[7] spatiotemporal chaos,[8] and water–oil swirling flow.[9]

Topological representations in fluid dynamics can be categorized into several groups, including vortex and helicity, stability in dynamical systems, phase-transition, and constitutive relations. For example, the topology of vortex and helicity provides a fundamental knowledge of the propensity of flows to form vortices or coherent structures in classical fluids.[10–15] The topological study of the stability of dynamical systems can provide a basic understanding of time-periodic vortex ring flows.[16] Phase-transition, which refers to transitions in a system from one state to another, can also be studied from the viewpoint of topology. For example, the phase transition between a liquid and a crystal involves a transition in topological order from the continuous translation symmetry of the liquid to the discrete symmetry of the crystal.[17]

Constitutive equations (or relations) in fluid dynamics describe the thermo-fluidic behavior of a fluid subjected to certain thermodynamic driving forces such as spatial gradients of velocity and temperature. They are combined with the physical conservation laws of mass, momentum, and energy and initial and boundary conditions to solve specific physical problems. In most cases, constitutive equations—indispensable in fluid dynamics—are derived with the intention of describing the generic property of fluids.

The most well-known constitutive equations in fluid dynamics are the two-century-old Navier–Stokes and Fourier (called NSF hereafter) relations.[18] Their basic forms were derived in 1822, and they are considered the *de facto* mathematical models for every possible flow problem. Nonetheless, the topological representations of the first-order constitutive relations, such as the NSF relations, were found to be trivial, since the NSF relations are linear and thus do not require topological development beyond the obvious linear topology. This fact explains why there was virtually no previous study on the application of topological ideas to the constitutive equations in fluid dynamics.

However, there are caveats associated with the present status. A vital assumption, near the local-thermal-equilibrium (LTE), was introduced in the derivation of the NSF relations, and as a result, their validity may be seriously questioned in flows whose status is not near the LTE. Indeed, there have been recent active studies on the physics of fluids in high thermal nonequilibrium. They involve various disciplines, from gaseous motion in rarefied, micro- and nano-scale,[19–22] hypersonic conditions[23–27] to electron transport in semi-conductor devices[28,29] and non-Newtonian viscoelastic fluids,[30–32] such as polymer solutions, lubricant fluids, and complex fluids. Moreover, other problems such as the odd viscosity in chiral active fluids composed of self-spinning objects[33,34] and relativistic high-energy hydrodynamics[35,36] are known to require higher-order theories beyond the conventional NSF relations.

Another vital assumption behind the NSF relations is the so-called Stokes's hypothesis, introduced by Stokes[37] in 1845, in which bulk viscosity μ_b vanishes (λ and μ being the second coefficient of viscosity and the shear viscosity of the fluid, respectively),

$$\mu_b \equiv \lambda + \frac{2}{3}\mu = 0, \quad \text{equivalently, } \lambda = -\frac{2}{3}\mu. \tag{1}$$

While the Stokes's hypothesis is certainly legitimate in the case of monatomic gases such as argon, there is ever increasing evidence that now indicates this is not the case for diatomic and polyatomic gases[38–49]—such as nitrogen (or air), methane, and carbon dioxide.

Examples of such cases include the inner structure of strong shock waves in diatomic gases, and hypersonic entry into the Mars atmosphere, which consists mostly of carbon dioxide. In fact, a recent experimental study on the second-mode instability in the laminar-to-turbulence transition in hypersonic boundary layers[43] showed that, for a real diatomic gas, the growth and decay of the second mode is accompanied by a dilatation process, which leads to a 50% increase in dilatation dissipation, in contrast to the Stokes hypothesis. Moreover, direct numerical simulation (DNS) studies of turbulence by Pan and Johnsen[45] have shown that bulk viscosity significantly increases the decay rate of turbulent kinetic energy and dilatation is reduced by over two orders of magnitude within the first two eddy-turnover times. Furthermore, Singh *et al.*[46] found a significant increase in enstrophy with increasing bulk viscosity, which is directly related to the rotational mode of gas molecules.

These recent developments point out to an interesting question: What happens to the topology of constitutive equations if two vital assumptions in the NSF relations—the near LTE and Stokes's hypothesis—are removed?

A first hint to this question may be found in an analytical study by Myong[50] on the role of the first- and second-order constitutive relations in a force-driven compressible Poiseuille gas flow. It was shown that a convex topological profile with a central maximum in pressure is predicted for diatomic gases, in stark contrast to the concave topological profile with a central minimum in pressure for a monatomic gas. The pressure profile becomes less concave as the bulk viscosity increases, and across a critical point, it turns into a convex shape, clearly indicating the possibility of using topological ideas to unravel the ultimate origin of such non-intuitive behavior.

The study of the topology of constitutive equations beyond the first-order level requires proper master kinetic equations for diatomic and polyatomic gases. In recent decades, several such kinetic models have been developed, notably the Bhatnagar-Gross-Krook (BGK) Boltzmann model equations,[51,52] Wang–Chang–Uhlenbeck (WCU) model,[53] Fokker–Planck based kinetic model,[54] and Rykov model.[55,56] However, a common drawback was identified in these kinetic models for diatomic and polyatomic gases in that they do not reduce to the Boltzmann kinetic equation for a monatomic gas when translational–internal (rotational) energy exchange is absent. For this reason, an alternative approach to smoothly extend the original Boltzmann kinetic equation to diatomic and (linear) polyatomic gases, the so-called Boltzmann–Curtiss kinetic equation,[57,58] will be considered in this study on the topological representation of the constitutive relations of gas flows.

The Boltzmann–Curtiss kinetic equation additionally introduces the angular momentum and azimuth angle associated with the rotational mode of molecules to the kinetic formulation. As a result, an additional term, the change in the distribution function in the azimuth angle, appears in the kinematic description of the movement of molecules. At the same time, the Boltzmann treatment of collision integral based on the concept of gain and loss remains the same, except for the appearance of the magnitude of the angular momentum and azimuth angle in the integration in phase space. Therefore, similar to the original Boltzmann kinetic equation for monatomic gases, the high-order constitutive equations for diatomic and polyatomic gases can be systematically derived

from the Boltzmann–Curtiss kinetic equation on the basis of Eu's modified moment method[59,60] and Myong's closing-last balanced closure.[61]

Among possible high-order constitutive equations, the second-order constitutive relations for diatomic gases were studied numerically in the context of multi-dimensional computational models.[21] An important result obtained from this study was that the second-order constitutive relations between stresses (and heat flux) and the velocity gradient (and the temperature gradient) are highly nonlinear and strongly coupled in the states far from the LTE. The second-order constitutive relations for a monatomic gas have also been validated for the force-driven Poiseuille gas flow by the deterministic atomic-level microscopic molecular dynamics (MD) simulation of Rana *et al.*[62]

Encouraged by these developments, in this study, we aim to comprehensively investigate the topology of the second-order constitutive equations beyond the first-order NSF equations built on the near LTE assumption and Stokes's hypothesis. Emphasis is placed on the effects of thermal non-equilibrium and the bulk viscosity associated with the viscous excess normal stress on diatomic and polyatomic gases and their interplay in the topological space. Furthermore, we attempt to investigate the trajectory of the shock structure solution on the topology of second-order constitutive equations for diatomic and polyatomic gases. *To the authors' best knowledge, no study has been reported in the past to explain the topology of the high-order constitutive equations for diatomic and polyatomic gases in the field of fluid dynamics.*

Toward these goals, we first consider in depth the Boltzmann–Curtiss kinetic equation for diatomic and polyatomic gases and derive the second-order constitutive equations. The topological representations of the first-order and second-order constitutive equations for diatomic and polyatomic gases are then systematically studied to highlight the differences with monatomic gases. A comparative study of the cross-sectional features of topology is also presented to characterize the velocity shear and compression–expansion flows. Furthermore, the role of the second-order constitutive equations in the shock structure problem is studied by combining shock structure solutions with the topological representation of the constitutive equations. Finally, the effects of the Mach number and bulk viscosity on the topology of the shock structure solution are investigated.

II. SECOND-ORDER CONSTITUTIVE MODEL FOR DIATOMIC AND POLYATOMIC GASES

A. Boltzmann–Curtiss kinetic equation and the exact conservation laws for diatomic and polyatomic gases

The Boltzmann–Curtiss kinetic equation for diatomic (and linear polyatomic) molecules with a moment of inertia I_m and an angular momentum $\mathbf{j}$ can be expressed[57] as follows, when there is no external field:

$$\left(\frac{\partial}{\partial t}+\mathbf{v}\cdot\nabla+\frac{j}{I_m}\frac{\partial}{\partial\psi}\right)f(\mathbf{v},\mathbf{r},\mathbf{j},\psi,t)=R[f], \tag{2}$$

where f, $\mathbf{v}$, $\mathbf{r}$, ψ, j, and $R[f]$ represent the distribution function, the particle velocity, the particle position, the azimuthal angle associated with the orientation of the particle, the magnitude of the angular momentum vector $\mathbf{j}$, and the collision integral, respectively. When the angular momentum of the molecule related to the rotational mode is ignored, the Boltzmann–Curtiss kinetic equation recovers the original Boltzmann kinetic equation for a monatomic gas,

$$\left(\frac{\partial}{\partial t}+\mathbf{v}\cdot\nabla\right)f(\mathbf{v},\mathbf{r},t)=C[f],$$

where $C[f]$ represents the Boltzmann collision integral of the interaction between two particles.

There are two different sets of macroscopic variables: the conserved variables (ρ, $\rho\mathbf{u}$, ρE) and the non-conserved variables ($\mathbf{\Pi}$, Δ, $\mathbf{Q}$), where $\mathbf{u}$ is the velocity vector, E is the total energy density, while $\mathbf{\Pi}$, Δ, and $\mathbf{Q}$ represent the shear stress tensor, the excess normal stress, and the heat flux, respectively. These variables can be defined by a statistical formula

$$\phi^{(k)}=\left\langle h^{(k)}f\right\rangle, \tag{3}$$

where the angular bracket denotes the integration over the variables $\mathbf{v}$ and j. The $h^{(k)}$ indicates the molecular expressions for moments. The leading elements of the set of the conserved and non-conserved variables are defined as[60]

$$\begin{gathered}\phi^{(1)}=\rho,\quad \phi^{(2)}=\rho\mathbf{u},\quad \phi^{(3)}=\rho E,\\ \phi^{(4)}=\mathbf{\Pi}=[\mathbf{P}]^{(2)},\quad \phi^{(5)}=\Delta=\frac{1}{3}\mathrm{Trace}\,\mathbf{P}-p,\quad \phi^{(6)}=\mathbf{Q}\end{gathered} \tag{4}$$

with the molecular expressions corresponding to this set

$$\begin{gathered}h^{(1)}=m,\quad h^{(2)}=m\mathbf{v},\quad h^{(3)}=\frac{1}{2}mC^2+H_{rot},\\ h^{(4)}=[m\mathbf{CC}]^{(2)},\quad h^{(5)}=\frac{1}{3}mC^2-p/n,\\ h^{(6)}=\frac{1}{2}mC^2+H_{rot}-m\hat{h},\end{gathered} \tag{5}$$

where m is the molecular mass, $\mathbf{C}=\mathbf{v}-\mathbf{u}$ is the peculiar velocity of the molecule, n is the number density per unit mass, $\hat{h}$ is the enthalpy density per unit mass, and $H_{rot}=j^2/2I_m$ is the rotational Hamiltonian of the particle. The viscous stresses $\mathbf{\Pi}$ and Δ are related to the stress tensor $\mathbf{P}$ through the relation

$$\mathbf{P}=(p+\Delta)\mathbf{I}+\mathbf{\Pi}. \tag{6}$$

Here, $\mathbf{I}$ is the unit second rank tensor and $p=nk_BT=\rho RT$ is the equation of state. The symbol $[\mathbf{A}]^{(2)}$ denotes the traceless symmetric part of the second-rank tensor $\mathbf{A}$,

$$[\mathbf{A}]^{(2)}=\frac{1}{2}\left(\mathbf{A}+\mathbf{A}^t\right)-\frac{1}{3}\mathbf{I}\,\mathrm{Trace}\,\mathbf{A}. \tag{7}$$

The conservation laws of mass, momentum, and total energy for diatomic and polyatomic gases can be derived directly from the Boltzmann–Curtiss kinetic equation by noting that the molecular expressions for conserved variables (5) are collision invariants, and thus, there is no dissipation term, i.e., $\langle h^{(1,2,3)}R[f]\rangle=0$. After differentiating the statistical definition of the conserved variables with time and combining them with the Boltzmann–Curtiss equation, the following conservation laws, all of which are an *exact* consequence of the Boltzmann–Curtiss kinetic equation, can be derived:[21,60]

$$\frac{\partial}{\partial t}\begin{bmatrix}\rho\\ \rho\mathbf{u}\\ \rho E\end{bmatrix}+\nabla\cdot\begin{bmatrix}\rho\mathbf{u}\\ \rho\mathbf{uu}+p\mathbf{I}\\ (\rho E+p)\mathbf{u}\end{bmatrix}+\nabla\cdot\begin{bmatrix}0\\ \mathbf{\Pi}+\Delta\mathbf{I}\\ (\mathbf{\Pi}+\Delta\mathbf{I})\cdot\mathbf{u}+\mathbf{Q}\end{bmatrix}=0. \tag{8}$$

After the following dimensionless variables and parameters are introduced,

$$t^* = \frac{t}{(L/u_r)}, \quad \boldsymbol{x}^* = \frac{\boldsymbol{x}}{L}, \quad \mu^* = \frac{\mu}{\mu_r}, \quad k^* = \frac{k}{k_r},$$
$$\boldsymbol{u}^* = \frac{\boldsymbol{u}}{u_r}, \quad p^* = \frac{p}{p_r}, \quad \rho^* = \frac{\rho}{\rho_r},$$
$$T^* = \frac{T}{T_r}, \quad C_p^* = \frac{C_p}{C_{pr}}, \quad E^* = \frac{E}{u_r^2}, \quad \boldsymbol{\Pi}^* = \frac{\boldsymbol{\Pi}}{(\mu_r u_r/L)},$$
$$\Delta^* = \frac{\Delta}{(\mu_{b_r} u_r/L)}, \quad \mathbf{Q}^* = \frac{\mathbf{Q}}{(k_r \Delta T/L)}, \tag{9}$$

where the subscript r stands for the reference state, L denotes the characteristic length, C_p denotes the heat capacity per mass at constant pressure, μ, μ_b, and k are the Chapman–Enskog shear viscosity, the bulk viscosity, and the thermal conductivity, respectively, the non-dimensional conservation laws for diatomic and polyatomic gases (with the asterisks omitted for notational brevity) can be written as[21]

$$\frac{\partial}{\partial t}\begin{bmatrix}\rho\\ \rho\mathbf{u}\\ \rho E\end{bmatrix} + \nabla\cdot\begin{bmatrix}\rho\mathbf{u}\\ \rho\mathbf{u}\mathbf{u} + \frac{1}{\gamma M^2}p\mathbf{I}\\ \left(\rho E + \frac{1}{\gamma M^2}p\right)\mathbf{u}\end{bmatrix} + \nabla\cdot\frac{1}{\mathrm{Re}}\begin{bmatrix}0\\ \boldsymbol{\Pi} + f_b\Delta\mathbf{I}\\ (\boldsymbol{\Pi} + f_b\Delta\mathbf{I})\cdot\mathbf{u} + \frac{1}{Ec\,\mathrm{Pr}}\mathbf{Q}\end{bmatrix} = 0. \tag{10}$$

Here, the dimensionless parameters such as the Mach number (M), Reynolds number (Re), Eckert number (Ec), and Prandtl number (Pr) can be defined as follows:

$$M \equiv \frac{u_r}{\sqrt{\gamma R T_r}}, \ \mathrm{Re} \equiv \frac{\rho_r u_r L}{\mu_r}, \ Ec \equiv (\gamma-1)M^2, \ \mathrm{Pr} \equiv \frac{c_{p_r}\mu_r}{k_r}, \ f_b = \frac{\mu_{b_r}}{\mu_r}. \tag{11}$$

The specific heat ratio γ is assumed to be 5/3 for argon gas, 7/5 for nitrogen gas, 1.289 for methane gas, and 1.29 for carbon dioxide. The value of the Prandtl number (Pr) may be calculated through Eucken's relation

$$\mathrm{Pr} = \frac{4\gamma}{9\gamma - 5}. \tag{12}$$

B. Zeroth-order Boltzmann–Curtiss-based (Euler) constitutive model

The zeroth-order Boltzmann–Curtiss-based (Euler) constitutive model is a direct consequence of assuming local thermal equilibrium, that is, the Maxwellian distribution function.[59] Therefore, the zeroth-order Boltzmann–Curtiss-based constitutive model of the shear stress, the excess normal stress, and the heat flux is reduced to the following simple relations:

$$\boldsymbol{\Pi} = 0, \quad \Delta = 0, \quad \mathbf{Q} = 0. \tag{13}$$

C. First-order Boltzmann–Curtiss-based (Navier–Fourier) constitutive model

After differentiating the statistical definition of the non-conserved variables $\phi^{(4,5,6)} = \langle h^{(4,5,6)} f\rangle$ with time and combining them with the Boltzmann–Curtiss equation, the following first-order Boltzmann–Curtiss-based constitutive model of the shear stress, the excess normal stress, and the heat flux can be obtained:

$$\boldsymbol{\Pi} = -2\mu[\nabla\mathbf{u}]^{(2)}, \quad \Delta = -\mu_b\nabla\cdot\mathbf{u}, \quad \mathbf{Q} = -k\nabla T. \tag{14}$$

During this process, first-order closure was applied. Furthermore, once the Stokes's hypothesis (1) is applied, that is, $\mu_b = 0$, the conservation laws in conjunction with the first-order Navier-Fourier (NF) constitutive equations (14) are reduced to the following well-known NSF equations:

$$\frac{\partial}{\partial t}\begin{bmatrix}\rho\\ \rho\mathbf{u}\\ \rho E\end{bmatrix} + \nabla\cdot\begin{bmatrix}\rho\mathbf{u}\\ \rho\mathbf{u}\mathbf{u} + p\mathbf{I}\\ (\rho E + p)\mathbf{u}\end{bmatrix} - \nabla\cdot\begin{bmatrix}0\\ 2\mu[\nabla\mathbf{u}]^{(2)}\\ 2\mu[\nabla\mathbf{u}]^{(2)}\cdot\mathbf{u} + k\nabla T\end{bmatrix} = 0. \tag{15}$$

It should be noted that these first-order linear relations were obtained after very crude first-order approximations; all kinematic terms except for the thermodynamic force term were neglected in the moment equations, and the collision-related dissipation terms $\langle h^{(4,5,6)} R[f]\rangle$ were linearized.

In these expressions, the following Chapman–Enskog linear transport coefficients can be employed:

$$\mu = T^s, \ \mu_b = f_b\mu, \ k = T^s, \tag{16}$$

where s stands for the index of the inverse power laws of gas molecules, given as

$$s = \frac{1}{2} + \frac{2}{(\nu - 1)}.$$

Here, the parameter ν is the exponent of the inverse power laws for the gas particle interaction potentials. The value of s was assumed to be 0.81 for argon gas, 0.78 for nitrogen, 0.84 for methane gas, and 0.93 for carbon dioxide gas.[63] The factor $f_b = \mu_b/\mu$ is the ratio of the bulk viscosity to the shear viscosity. Its value may be experimentally determined using a sound wave absorption measurement. The f_b values for argon, nitrogen, methane, and carbon dioxide gases were considered to be 0.0, 0.8, 1.33, and 1000, respectively, based on experiments.[64]

D. Second-order Boltzmann–Curtiss-based constitutive model: Closing-last balanced closure and cumulant expansion

Similarly, the high-order constitutive model can be derived by first differentiating the statistical definition of the non-conserved variables $\phi^{(4,5,6)}$ with time and then combining them with the Boltzmann–Curtiss kinetic equation,

$$\rho\frac{D}{Dt}\left(\frac{\boldsymbol{\Pi}}{\rho}\right) + \nabla\cdot\boldsymbol{\Psi}^{(\Pi)} + 2[\boldsymbol{\Pi}\cdot\nabla\mathbf{u}]^{(2)} + 2(\Delta + p)[\nabla\mathbf{u}]^{(2)} = \left\langle h^{(4)} R[f]\right\rangle,$$
$$\rho\frac{D}{Dt}\left(\frac{\Delta}{\rho}\right) + \nabla\cdot\boldsymbol{\Psi}^{(\Delta)} + 2\gamma'(\boldsymbol{\Pi} + \Delta\mathbf{I}) : \nabla\mathbf{u} + \frac{2}{3}\gamma' p\nabla\cdot\mathbf{u} = \left\langle h^{(5)} R[f]\right\rangle,$$
$$\rho\frac{D}{Dt}\left(\frac{\mathbf{Q}}{\rho}\right) + \nabla\cdot\boldsymbol{\Psi}^{(\mathbf{Q})} + \boldsymbol{\Psi}^{(\mathrm{P})} : \nabla\mathbf{u} + \frac{D\mathbf{u}}{Dt}\cdot\boldsymbol{\Pi} + \mathbf{Q}\cdot\nabla\mathbf{u} + (\boldsymbol{\Pi} + \Delta\mathbf{I} + p\mathbf{I})\cdot C_p\nabla T = \left\langle h^{(6)} R[f]\right\rangle. \tag{17}$$

Here, $\gamma' = (5 - 3\gamma)/2$ and $\boldsymbol{\Psi}^{(\Pi,\Delta,\mathbf{Q},\mathbf{P})}$ represent the open high-order terms of the shear stress, the excess normal stress, and the heat flow, respectively.

However, it turns out that the derivation of the second-order constitutive model is extremely difficult, mainly due to two

TABLE I. Physical properties of monatomic, diatomic, and polyatomic gases.

Gases	Specific heat ratio (γ)	Bulk viscosity ratio (f_b)	Prandtl number (Pr)	Viscosity index (s)	Gas constant (R)	Viscosity coefficient (μ_{ref})
Maxwellian	1.667	0.0	0.75	1.0	...	...
Argon	1.667	0.0	0.667	0.81	208.24	2.117×10^{-5}
Nitrogen	1.4	0.8	0.7368	0.74	296.91	1.656×10^{-5}
Methane	1.3125	1.33	0.7706	0.84	518.0	1.024×10^{-5}
Carbon dioxide	1.2985	1000	0.777	0.93	188.87	1.38×10^{-5}

fundamental issues: the so-called closure problem and accurate treatment of the complicated dissipation terms $\langle h^{(4,5,6)} R[f] \rangle$, both of which have remained unsolved for several decades. In order to accurately calculate the dissipation terms while making the underlying theory compatible with the second law of thermodynamics, Eu in 1980 proposed a canonical distribution function in the exponential form, instead of the usual polynomial form, after recognizing the logarithmic form of the non-equilibrium entropy production.[60]

On the other hand, Myong in 2014 developed a new closure theory, known as "*closing-last balanced closure*," from a keen observation of the fact that, when closing open terms in the moment equations derived from the kinetic equation, the number of places to be closed was two (movement and interaction), rather than one (movement only), having been misled by the Maxwellian molecule assumption in the previous theory.[61] For example, there are two terms requiring closure in the constitutive equation of viscous stress (17): $\nabla \cdot \boldsymbol{\Psi}^{(\boldsymbol{\Pi})}$ and $\langle h^{(4)} R[f] \rangle$. Therefore, the order of approximations in handling the two terms—kinematic (movement) and dissipation (interaction) terms—must be the same to satisfy balancing, for instance, the second-order for both terms, thus achieving a balance between the kinematic and collision term approximation, namely, the second-order closure for the kinematic terms,

$$\nabla \cdot \boldsymbol{\Psi}^{(\boldsymbol{\Pi})} = \nabla \cdot \boldsymbol{\Psi}^{(\Delta)} = \nabla \cdot \boldsymbol{\Psi}^{(\mathbf{Q})} + \boldsymbol{\Psi}^{(\mathrm{P})} : \nabla \mathbf{u} = 0,$$

while maintaining the same second-order closure for $\langle h^{(4,5,6)} R[f] \rangle$. In this balanced closure framework, the third-order closure for $\langle h^{(4,5,6)} R[f] \rangle$ is not necessary; in fact, such higher closure can make the problem worse, in particular, in the case of the high Mach number shock structure problem.

Once these two tenets—Eu's cumulant expansion based on the canonical distribution function in the exponential form to the explicit calculation of the dissipation term and the aforementioned closing-last balanced closure—are applied to the moment equations (17) and after introducing the so-called adiabatic approximation derived from the observation that the relaxation times of the non-conserved variables are very short, being of the order of 10^{-10} s,[19] the following second-order constitutive model can be derived from the Boltzmann–Curtiss kinetic equation:[21]

$$\begin{aligned} \left[\hat{\boldsymbol{\Pi}} \cdot \nabla \hat{\boldsymbol{u}}\right]^{(2)} + \left(f_b \hat{\Delta} + 1\right) \hat{\boldsymbol{\Pi}}_0 &= \hat{\boldsymbol{\Pi}} q_{2nd}(c\hat{R}), \\ \frac{3}{2} f_b \left(\hat{\boldsymbol{\Pi}} + f_b \hat{\Delta} \mathbf{I}\right) : \nabla \hat{\boldsymbol{u}} + \hat{\Delta}_0 &= \hat{\Delta} q_{2nd}(c\hat{R}), \\ \hat{\boldsymbol{\Pi}} \cdot \hat{\mathbf{Q}}_0 + \left(f_b \hat{\Delta} + 1\right) \hat{\mathbf{Q}}_0 &= \hat{\mathbf{Q}} q_{2nd}(c\hat{R}). \end{aligned} \tag{18}$$

All terms in Eq. (18) were normalized by introducing proper variables and parameters,

$$\begin{gathered} \hat{\boldsymbol{\Pi}} \equiv \frac{N_\delta}{p} \boldsymbol{\Pi}, \quad \hat{\Delta} \equiv \frac{N_\delta}{p} \Delta, \quad \hat{\mathbf{Q}} \equiv \frac{N_\delta}{p} \frac{\mathbf{Q}}{\sqrt{T/(2\varepsilon)}}, \quad \nabla \hat{\boldsymbol{u}} \equiv -2\mu \frac{N_\delta}{p} \nabla \mathbf{u}, \\ N_\delta \equiv \frac{\mu_r u_r / L}{p_r} = \frac{\gamma M^2}{\mathrm{Re}} = KnM \sqrt{\frac{2\gamma}{\pi}}, \quad \varepsilon \equiv \frac{1}{Ec\,\mathrm{Pr}} \frac{1}{T_r/\Delta T}. \end{gathered} \tag{19}$$

The caret ($\hat{}$) over a symbol represents a quantity whose dimension is the ratio of viscous stress to pressure. Note that the relationships in the second-order Boltzmann–Curtiss-based constitutive model (18) are highly nonlinear and coupled for the given velocity and temperature gradients. The values of $\boldsymbol{\Pi}_0$, Δ_0, and $\mathbf{Q}_0$ are determined by the linear Newtonian law of shear and bulk viscosity and by the linear Fourier law of heat conduction, respectively, given in (14).

On the other hand, by combining with the Rayleigh–Onsager dissipation function,[65] $\hat{R}$, the second-order nonlinear coupling factor $q_{2nd}(c\hat{R})$ in (18) can be expressed as follows:

$$q_{2nd}(c\hat{R}) = \frac{\sinh(c\hat{R})}{c\hat{R}}, \quad \hat{R}^2 \equiv \hat{\boldsymbol{\Pi}} : \hat{\boldsymbol{\Pi}} + \frac{2\gamma'}{f_b} \hat{\Delta}^2 + \hat{\mathbf{Q}} \cdot \hat{\mathbf{Q}}. \tag{20}$$

The constant c, which is given by $c = [2\sqrt{7/5}\, A_2(\nu)\Gamma(4 - 2/\nu_{-1})]^{1/2}$, has a value between 1.0138 (Maxwellian) and 1.2232 ($\nu = 3$), for instance, 1.018 for the nitrogen gas molecule.[21] The tabulated values of $A_2(\nu)$ are available in the literature.[63]

Note that once $q_{2nd}(c\hat{R})$ is replaced by the first-order closure, that is, $q_{1st} = 1$, and all coupled terms in the left-hand side of (18) are neglected, the corresponding constitutive models exactly recover the NF models (14). The physical properties of monatomic, diatomic, and polyatomic gases are given in Table I.

III. TOPOLOGICAL REPRESENTATION OF THE SECOND-ORDER BOLTZMANN-CURTISS-BASED CONSTITUTIVE MODEL

A. Topology of the second-order Boltzmann–Curtiss-based constitutive model in velocity shear: A conic section

In order to investigate the topology of the Boltzmann–Curtiss-based constitutive model, we consider monatomic, diatomic, and (linear) polyatomic gases. In general, the second-order constitutive model (18) consists of nine equations of (Π_{xx}, Π_{xy}, Π_{xz}, Π_{yy}, Π_{yz}, Π_{zz}, Q_x, Q_y, Q_z) for 14 known parameters (p, T, ∇u, ∇v, ∇w, ∇T). Because of the nine-dimensional topology in phase space and its

highly nonlinear and coupled nature, investigating its topology in any meaningful way seems very difficult. Nevertheless, the topology can be rather efficiently investigated based on the concept of decomposition, which was first introduced by Myong.[20]

In general, the viscous stress and heat flux components on a line (or interface) in the physical plane induced by the thermodynamic forces of velocity and temperature gradients can be decomposed (or split) into two elementary subsets: one on the velocity shear flow and another on the gaseous compression and expansion flow. In the subset of *velocity shear* flow, the stresses (Π_{xx}, Π_{xy}, Δ) induced by the thermodynamic force $v_x \equiv \partial v/\partial x$ can be determined from (18)–(20) as follows:

$$\begin{aligned} \hat{\Pi}_{xx} q_{2nd}(c\hat{R}) &= -\frac{2}{3}\hat{\Pi}_{xy}\hat{\Pi}_{xy_0}, \\ \hat{\Pi}_{xy} q_{2nd}(c\hat{R}) &= \left(1 + f_b\hat{\Delta} + \hat{\Pi}_{xx}\right)\hat{\Pi}_{xy_0}, \\ \hat{\Delta} q_{2nd}(c\hat{R}) &= 3f_b\,\hat{\Pi}_{xy}\hat{\Pi}_{xy_0}. \end{aligned} \tag{21}$$

After some manipulation, the following equations on variables $\hat{\Pi}_{xx}$ and $\hat{\Delta}$ can be derived:

$$\begin{aligned} \hat{\Pi}_{xx} q_{2nd}^2(c\hat{R}) &= -\frac{2}{3}\left[\left(1 - \frac{9}{2}f_b^2\right)\hat{\Pi}_{xx} + 1\right]\hat{\Pi}_{xy_0}^2, \\ \hat{\Delta} &= -\frac{9}{2}f_b\hat{\Pi}_{xx}. \end{aligned} \tag{22}$$

Furthermore, when the first two components of equations in (21) are divided by each other, the nonlinear coupling factor $q_{2nd}(c\hat{R})$ and the driving force $\hat{\Pi}_{xy_0}$ are canceled out, leaving only a common kinematic viscous stress constraint,

$$\frac{2}{3}\hat{\Pi}_{xy}^2 + \left(1 - \frac{9}{2}f_b^2\right)\hat{\Pi}_{xx}^2 + \hat{\Pi}_{xx} = 0,$$

or

$$\hat{\Pi}_{xy} = sign\left(\hat{\Pi}_{xy_0}\right)\left\{-\frac{3}{2}\left[\left(1 - \frac{9}{2}f_b^2\right)\hat{\Pi}_{xx} + 1\right]\hat{\Pi}_{xx}\right\}^{1/2}. \tag{23}$$

Combining all these relations, the dissipation function (20) reduces to

$$\hat{R}^2 = 3\hat{\Pi}_{xx}\left[\left(1 + \frac{9}{2}f_b(f_b + 3\gamma')\right)\hat{\Pi}_{xx} - 1\right]. \tag{24}$$

Surprisingly, when the kinematic viscous stress constraint (23) is expressed in an instructive form using the following simple notation:

$$x \equiv \hat{\Pi}_{xx} = \frac{\Pi_{xx}}{p},\ y \equiv \hat{\Pi}_{xy} = \frac{\Pi_{xy}}{p},$$

the topology of the second-order Boltzmann–Curtiss-based constitutive model is governed by *a conic section* expressed as a second-degree polynomial equation in the phase space (x, y),

$$kx^2 + x + \frac{2}{3}y^2 = 0,\ \text{or}\ \frac{(x + 1/2k)^2}{1/4k^2} + \frac{y^2}{3/8k} = 1,\ \text{where}\ k = 1 - \frac{9}{2}f_b^2,$$

or

$$Ax^2 + Bxy + Cy^2 + Dx + Ey + F = 0, \tag{25}$$

where

$$A = k, B = 0,\ C = \frac{2}{3},\ D = 1, E = 0,\ F = 0.$$

A conic section is a curve obtained at the intersection of the surface of a cone with a plane and is classified into three types: the ellipse, the parabola, and the hyperbola.[66] The type of conic section is determined by the value of the eccentricity e. We obtain an ellipse for $0 < e < 1$ (a circle for $e = 0$), a parabola for $e = 1$, and a hyperbola for $e > 1$.

The conic section (25) can be also expressed in the matrix of the quadratic form,

$$\begin{aligned} &\begin{bmatrix} x & y \end{bmatrix}\begin{bmatrix} A & B/2 \\ B/2 & C \end{bmatrix}\begin{bmatrix} x \\ y \end{bmatrix} + \begin{bmatrix} D & E \end{bmatrix}\begin{bmatrix} x \\ y \end{bmatrix} + F = 0, \\ &A_{33} \equiv \begin{bmatrix} A & B/2 \\ B/2 & C \end{bmatrix} = \begin{bmatrix} k & 0 \\ 0 & 2/3 \end{bmatrix},\ \det A_{33} = \frac{2}{3}k, \end{aligned} \tag{26}$$

or in the matrix of the quadratic equation

$$\begin{aligned} &\begin{bmatrix} x & y & 1 \end{bmatrix}\begin{bmatrix} A & B/2 & D/2 \\ B/2 & C & E/2 \\ D/2 & E/2 & F \end{bmatrix}\begin{bmatrix} x \\ y \\ 1 \end{bmatrix} = 0, \\ &A_Q \equiv \begin{bmatrix} A & B/2 & D/2 \\ B/2 & C & E/2 \\ D/2 & E/2 & F \end{bmatrix} = \begin{bmatrix} k & 0 & 1/2 \\ 0 & 2/3 & 0 \\ 1/2 & 0 & 0 \end{bmatrix}, \\ &\det A_Q = -\tfrac{1}{6},\ \text{rank of}\ A_Q = 3. \end{aligned} \tag{27}$$

Since the determinant of A_Q is not zero for any value of f_b, the matrix representation of the present conic section is not degenerate and the types of conic sections can be easily determined by computing the determinant of A_{33} or the eccentricity.

The conic section is an ellipse for a positive determinant of A_{33} or $0 \le f_b < \sqrt{2}/3 \doteq 0.471$, a parabola for a zero determinant of A_{33} or $f_b = \sqrt{2}/3$, and a hyperbola for a negative determinant of A_{33} or $f_b > \sqrt{2}/3$. (When $A = C$ and $B = 0$, or $f_b = \sqrt{6}/9 \doteq 0.272$, it is a circle.)

Moreover, in the case of the present non-degenerate ellipse (with a positive determinant of A_{33} and a non-zero determinant of A_Q), we always have a real ellipse, since the following relation always holds:

$$(A + C)\det A_Q = \frac{3}{4}f_b^2 - \frac{5}{18} < 0.$$

Therefore, the topology of the second-order Boltzmann–Curtiss-based constitutive model is always smooth, having the derivatives of all orders everywhere in its conic section.

When the non-zero determinant of A_{33} or $f_b \neq \sqrt{2}/3$, a geometric center of the conic section exists, and such conic sections (ellipses and hyperbolas) are called central conic sections. The center of a conic section is a point that bisects all the chords of the conic section that pass through it. In the present case, a central (non-parabola) conic section can be written in the centered matrix form as

$$\begin{bmatrix} x - x_c & y - y_c \end{bmatrix}\begin{bmatrix} A & B/2 \\ B/2 & C \end{bmatrix}\begin{bmatrix} x - x_c \\ y - y_c \end{bmatrix} = \frac{-\det A_Q}{\det A_{33}} = \frac{1}{4k},$$

where

$$\begin{bmatrix} x_c \\ y_c \end{bmatrix} = \begin{bmatrix} A & B/2 \\ B/2 & C \end{bmatrix}^{-1}\begin{bmatrix} -D/2 \\ -E/2 \end{bmatrix} = \begin{bmatrix} -1/2k \\ 0 \end{bmatrix}. \tag{28}$$

Finally, the eccentricity of the present conic section can be written as

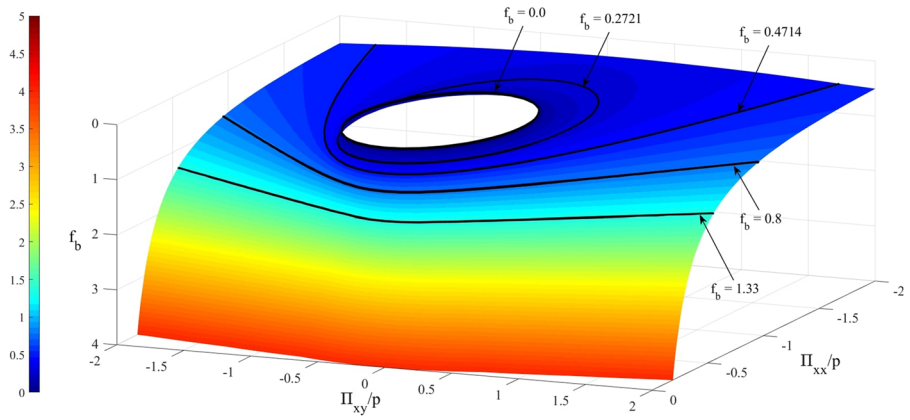

FIG. 1. Topology of the second-order Boltzmann–Curtiss-based constitutive models in the velocity shear flow problem in a phase space (Π_{xx}/p, Π_{xy}/p, f_b). With increasing f_b, the conic section varies from an ellipse for $0 \le f_b < 0.4714$ (including a circle for $f_b = 0.2721$) to a parabola for $f_b = 0.4714$ and then to a hyperbola for $f_b > 0.4714$. The topology of the conic section identified in the present second-order constitutive models has been echoed in the orbits of planets and comets in the Solar System governed by Kepler's laws.

$$e = \left[\frac{2\sqrt{(A-C)^2+B^2}}{A+C+\sqrt{(A-C)^2+B^2}}\right]^{1/2} = \begin{cases} \sqrt{\frac{2-27f_b^2}{6-27f_b^2}}, & \text{when } 0 \le f_b < \sqrt{6}/9 \\ \sqrt{\frac{27}{4}f_b^2 - \frac{1}{2}}, & \text{when } f_b > \sqrt{6}/9. \end{cases} \tag{29}$$

A topological representation of the second-order Boltzmann–Curtiss-based constitutive models (23), (25)–(28) in the velocity shear flow problem is given in a phase space (x, y, f_b) in Fig. 1. First of all, the bulk viscosity ratio f_b plays an essential role in determining the types of topology of the conic section. With increasing f_b, the conic section varies from an ellipse for $0 \le f_b < \sqrt{2}/3$ (including a circle for $f_b = \sqrt{6}/9$) to a parabola for $f_b = \sqrt{2}/3$ and then to a hyperbola for $f_b > \sqrt{2}/3$. On the other hand, the first-order Navier–Stokes-based constitutive models (14) are reduced to a simple plane, defined by $\Pi_{xx} = 0$ for all Π_{xy}, f_b (or $x = 0$ for all y, f_b), which makes a topological representation of the first-order constitutive models completely trivial. Figure 1 also shows the smooth surface (with the derivatives of all orders everywhere) consisting of continuous conic sections for varying f_b. Furthermore, it can be noted that, when $f_b \to \infty$, the conic section approaches asymptotically to a simple line defined as $\Pi_{xx} = 0$ for all Π_{xy}, which is a counter-intuitive outcome.

The existence of topology as shown in Fig. 1 implies that, when the diatomic and polyatomic gases with a specific value of f_b undergo velocity shear, the viscous shear and normal stresses (in reference to the hydrostatic pressure) are not independent at all and must be determined along a topological curve defined by a conic section (the ellipse, the parabola, or the hyperbola) in the phase space. The ultimate origin of the existence of the conic section can be traced to the second-order coupling of the viscous stress and the velocity gradient of kinematic nature, $\left[\hat{\mathbf{\Pi}} \cdot \nabla \hat{\mathbf{u}}\right]^{(2)}$, in the second-order Boltzmann–Curtiss constitutive model of the viscous stress (18). Because of this coupling, the term $kx^2 + 2y^2/3$ appears in Eq. (25) and, as a result, produces the rich topology of various conic sections.

The second-order Boltzmann–Curtiss-based constitutive models (24)–(29) in the velocity shear flow problem can be also represented in a different phase space (xp, yp, p)—equivalently, (Π_{xx}, Π_{xy}, p)—for a given value of f_b, as shown in Fig. 2. It is an ellipse cone for $f_b = 0$, while it is a hyperboloid for $f_b = 1$. In the case of a monatomic gas ($f_b = 0$), a similar type of ellipse cone was studied in the context of a phase-transition-like behavior in velocity slips in a cylindrical Couette flow.[67] Note from Fig. 2 that, as the pressure decreases, the ellipse cone keeps its topology, whereas the hyperboloid approaches a different topology, the straight lines defined as $\Pi_{xx} = -2|\Pi_{xy}|/\sqrt{21}$.

Figure 3 shows the trajectories of velocity-shear solutions on the topology of conic sections (an ellipse and a hyperboloid) in a phase space Π_{xx}, Π_{xy}, p for monatomic ($f_b = 0$) and diatomic ($f_b = 1$) gases. The second-order velocity-shear solutions were taken from previous analytical studies on a force-driven Poiseuille gas flow in a rectangular channel,[50,68] which had been validated for a monatomic gas using the deterministic atomic-level microscopic molecular dynamics (MD).[62]

The analytic solutions of pressure and shear and normal stresses in a velocity shear flow problem defined by Kn = 0.1 and

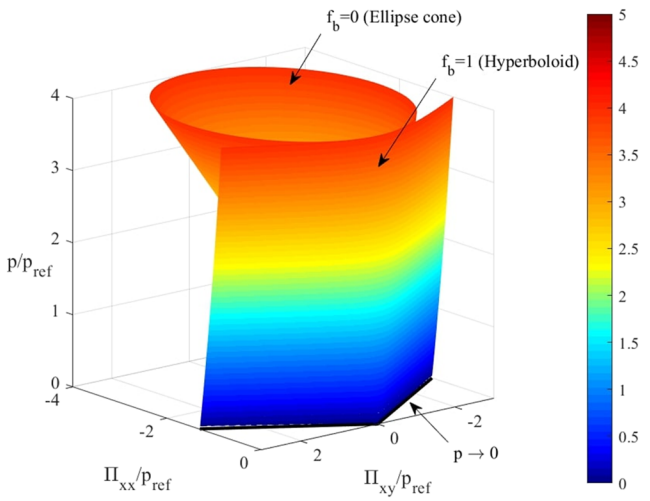

FIG. 2. Topology of the second-order Boltzmann–Curtiss-based constitutive models in the velocity shear flow problem in a phase space (Π_{xx}, Π_{xy}, p) for $f_b = 0$ and $f_b = 1$.

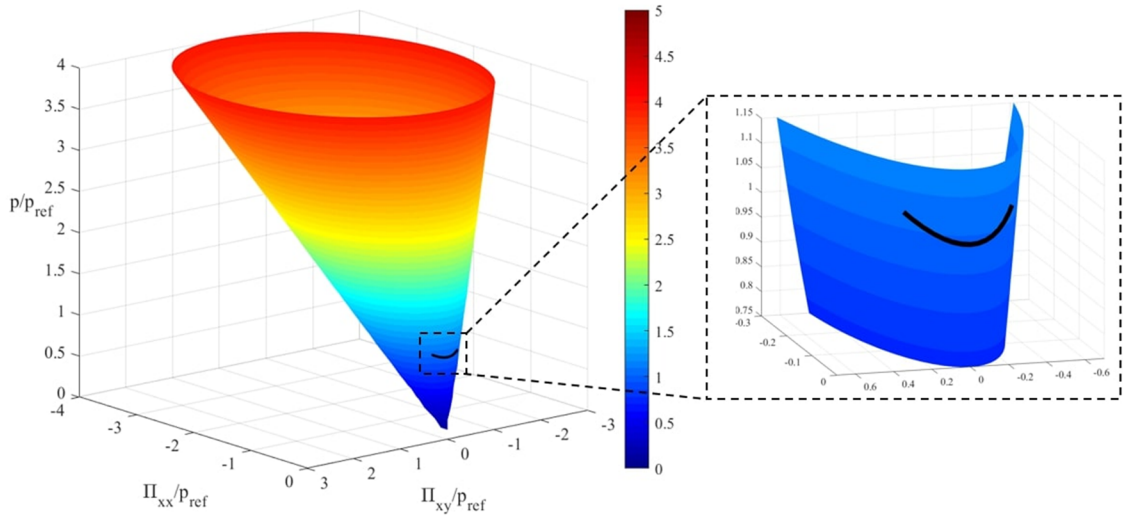

(a)

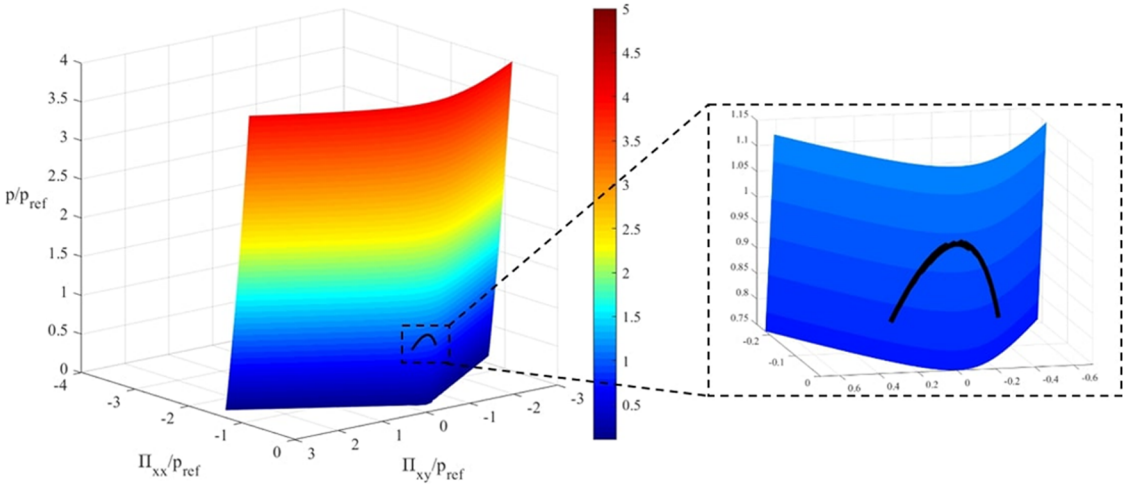

(b)

FIG. 3. Trajectories of velocity-shear solutions on the topology of conic sections (tangent trajectories on an ellipse cone and hyperbolic tangent trajectories on a hyperboloid) in a phase space (Π_{xx}, Π_{xy}, p): (a) f_b = 0.0 and (b) f_b = 1.0.

a force parameter $\varepsilon_{h_w} = 0.6$ are given by the tangent function on an ellipse cone and the hyperbolic tangent function on a hyperboloid,

$$\frac{p}{p_{ref}} = 1 + \tan^2 S_m^*, \quad \frac{\Pi_{xy}}{p_{ref}} = \sqrt{\frac{3}{2}} \tan S_m^*, \quad \frac{\Pi_{xx}}{p_{ref}} = -\tan^2 S_m^*,$$

where

$$S_m^* = \sqrt{\frac{2}{3}} T_{w_m}^* \varepsilon_{h_w} s^*, \tag{30}$$

$$\frac{p}{p_{ref}} = 1 - \tanh^2 S_d^*, \quad \frac{\Pi_{xy}}{p_{ref}} = \sqrt{\frac{3}{7}} \tanh S_d^*, \quad \frac{\Pi_{xx}}{p_{ref}} = -\frac{2}{7} \tanh^2 S_d^*,$$

where

$$S_d^* = \sqrt{\frac{7}{3}} T_{w_d}^* \varepsilon_{h_w} s^*, \tag{31}$$

in the domain $-0.5 \le s^* \le 0.5$ for monatomic ($f_b = 0$, $T_{w_m}^* = 0.942$) and diatomic ($f_b = 1$, $T_{w_d}^* = 0.962$) gases, respectively. The symbols p_{ref} and s^* represent the reference pressure in the middle of the channel and the dimensionless distance from the center to the wall of the channel, respectively.

The topology of conic sections has a long history in science. The most well-known conic sections are the *orbits of planets and comets* in the Solar System.[69] According to Kepler's laws of planetary motion, each object travels along an ellipse with the Sun at one focus.

In a two-body problem with inverse-square-law force, every orbit is a Kepler orbit. For example, the eccentricity of the Earth's orbit is about 0.0167. There are also many elliptic, parabolic, and hyperbolic comets in the Solar System. Halley's Comet has a value of 0.967, a highly eccentric elliptical orbit.

Another recent example of conic sections is the so-called *Dirac cones*, named after Paul Dirac.[70] They represent features that occur in some electronic band structures and describe the unusual electron transport properties of two-dimensional materials such as graphene and topological insulators. The cones are defined in a space consisting of two components of the crystal momentum and energy, (p_x, p_y, E). Dirac cones were experimentally observed in 2009 using angle-resolved photoemission spectroscopy on a graphite intercalation compound.[71]

Table II shows analogies among the second-order constitutive model, orbits of planets and comets, and Dirac cones. In particular, there is a direct analogy in the second-order constitutive model of diatomic and polyatomic gases and Kepler's laws of motion of the planets and comets. The bulk viscosity associated with the rotational mode of gas particles in reference to the shear viscosity plays a similar role in the energy associated with the angular motion of the planets and comets in reference to the gravitational potential energy. For example, the case of $f_b = 0.2722$ in the second-order constitutive model is equivalent to the case of $E = 0.9997E_{\min}$ in the Earth's orbit with the eccentricity $e = 0.0167$.

Until now, we have focused on the topology of the kinematic stress constraints (23), (25)–(28), which were derived by canceling out the driving force $\hat{\Pi}_{xy_0}$ from the second-order Boltzmann–Curtiss-based constitutive model of the velocity shear flow for diatomic and polyatomic gases (21). However, a further investigation is needed on the topology of the relationship between the unknown viscous stresses $\left(\hat{\Pi}_{xx}, \hat{\Pi}_{xy}, \hat{\Delta}\right)$ and the known thermodynamic force of $\hat{\Pi}_{xy_0}$. Even though the second-order constitutive model (21) involves highly nonlinear implicit algebraic equations,

TABLE II. Analogy among the second-order constitutive model, orbits of planets and comets, and Dirac cones.

	Second-order constitutive model in diatomic and polyatomic gases	Motion of the planets and comets in the two-body Kepler problem	Dirac cones in electronic band structures
Form of conic sections	$\left(1-\frac{9}{2}f_b^2\right)x^2 + x + \frac{2}{3}y^2 = 0$ $f_b = \frac{\text{bulk viscosity}}{\text{shear viscosity}}$	$\left(1-e^2\right)x^2 + 2epx + y^2 - p = 0$ $p = \frac{L^2}{Gm_1^2m_2^2/(m_1+m_2)}$ L: angular momentum G: gravitational constant $m_{1,2}$: mass $E_{\min} = -\frac{G^2m_1^3m_2^3/(m_1+m_2)}{2L}$	$\left(\frac{x}{2m^*/E} + \frac{\Delta^*}{E}\right)^2 + c_y^2y^2 - 1 = 0$ $p_{x,y}$: momentum Δ^*: merging gap m^* effective mass E: energy c_y: effective velocity
Definition of x and y	$x = \frac{\Pi_{xx}}{p}, \quad y = \frac{\Pi_{xy}}{p}$	$x = r\cos\theta, y = r\sin\theta$	$x = \frac{p_x^2}{E^2}, y = \frac{p_y}{E}$
Eccentricity	$e = \sqrt{\frac{27}{4}f_b^2 - \frac{1}{2}}$, for $f_b \geq \sqrt{6}/9$	$e = \sqrt{1-\frac{E}{E_{\min}}}$, for $E \geq E_{\min}(<0)$	$e = \sqrt{1-\frac{E^2}{E_{\max}^2}}$, for $E \leq E_{\max}(>0)$
Topological properties	$f_b = \sqrt{6}/9$; $e = 0$ (circle), $\sqrt{6}/9 < f_b < \sqrt{2}/3$; $0 < e < 1$ (ellipse), $f_b = \sqrt{2}/3$; $e = 1$ (parabola), $f_b > \sqrt{2}/3$; $e > 1$ (hyperbola)	$E = E_{\min}$; $e = 0$ (circle), $E_{\min} < E < 0$; $0 < e < 1$ (ellipse), $E = 0$; $e = 1$ (parabola), $E > 0$; $e > 1$ (hyperbola)	$E = E_{\max}$; $e = 0$ (circle), $0 < E < E_{\max}$; $0 < e < 1$ (ellipse), $E = 0$; $e = 1$ (parabola)
Direct analogy	$f_b \Leftrightarrow \frac{2\sqrt{3}}{9}\sqrt{\frac{1}{2}+e} = \frac{\sqrt{6}}{9}\sqrt{3-\frac{2E}{E_{\min}}}$ $f_b = 0.2722 \Leftrightarrow e_{\text{Earth}} = 0.0167$, $f_b = 0.2834 \Leftrightarrow e_{\text{Mercury}} = 0.2056$, $f_b = 0.4611 \Leftrightarrow e_{\text{Halley}} = 0.967$		

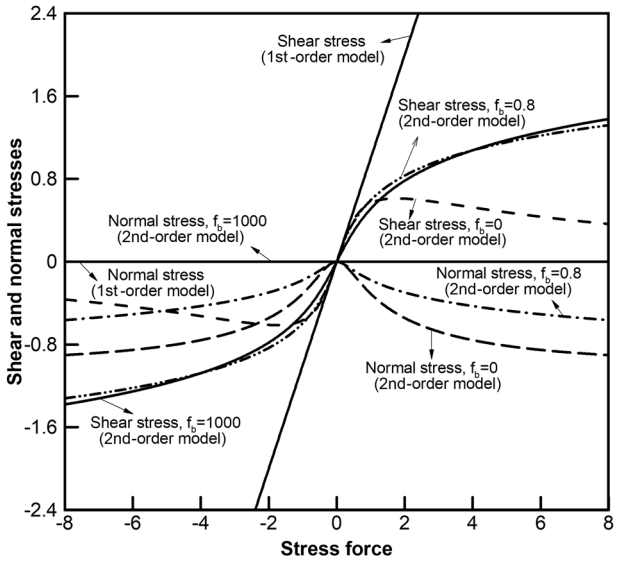

FIG. 4. First-order and second-order velocity-shear solutions of the Boltzmann–Curtiss based constitutive model for a driving stress force in monatomic, diatomic, and polyatomic gases. The horizontal axis represents the driving stress force $\hat{\Pi}_{xy_0}$, while the vertical axis represents the shear and normal stresses $\hat{\Pi}_{xy}$, $\hat{\Pi}_{xx}$.

they can be easily solved numerically in terms of the thermodynamic driving force $\hat{\Pi}_{xy_0}$ in conjunction with (23)–(28) using the method of iteration.[19,21]

Figure 4 shows such solutions of the second-order constitutive model for a given input in monatomic, diatomic, and polyatomic gases. The viscous shear stress $\hat{\Pi}_{xy}$ predicted by the second-order constitutive model recovers the first-order model near the origin, but it becomes highly nonlinear for all cases as the stress force (shear velocity gradient) increases. The second-order constitutive model shows the shear-thinning characteristics, yielding smaller shear stress compared to the first-order constitutive model. It also shows a completely different behavior for normal stress, producing non-zero normal stress values for a velocity gradient in shear flow. Interestingly, the general solutions of the second-order constitutive model also show asymptotic behavior with increasing degree of velocity shear, satisfying the free-molecular limit $\hat{\Pi}_{xx} + f_b\hat{\Delta} \to -1$ or $\Pi_{xx} + \Delta + p \to 0$. The ultimate origin of all these behaviors can be traced to the kinematic stress constraints in the second-order Boltzmann–Curtiss-based constitutive model, as shown in Figs. 1–3.

B. Topology of the second-order Boltzmann–Curtiss-based constitutive model in compression and expansion: Hyperbola and sinh-dominated topology

Based on the concept of decomposition, the second-order Boltzmann–Curtiss-based constitutive model can be decomposed into two elementary subsets: the velocity shear flow and the compression and expansion flow. In the case of compression and expansion flow, the viscous stresses and heat flux components (Π_{xx}, Δ, Q_x) induced by thermodynamic forces $u_x \equiv \partial u/\partial x$ and $T_x \equiv \partial T/\partial x$ can be determined from (18)–(20) as follows:

$$\begin{aligned}\hat{\Pi}_{xx}\, q_{2nd}(c\hat{R}) &= \left(1 + f_b\hat{\Delta} + \hat{\Pi}_{xx}\right)\hat{\Pi}_{xx_0},\\ \hat{\Delta}\, q_{2nd}(c\hat{R}) &= \left(1 + 3\left(f_b\,\hat{\Delta} + \hat{\Pi}_{xx}\right)\right)\hat{\Delta}_0,\\ \hat{Q}_x\, q_{2nd}(c\hat{R}) &= \left(1 + f_b\hat{\Delta} + \hat{\Pi}_{xx}\right)\hat{Q}_{x_0},\end{aligned} \tag{32}$$

where

$$\hat{R}^2 = \frac{3}{2}\hat{\Pi}_{xx}^2 + \frac{2\gamma'}{f_b}\hat{\Delta}^2 + \hat{Q}_x^2. \tag{33}$$

From the first-order Navier law (14), we obtain

$$\hat{\Delta}_0 = \frac{3}{4} f_b\, \hat{\Pi}_{xx_0}.$$

Similar to the velocity shear case, when the first two components of the equations in (32) are divided by each other, the nonlinear

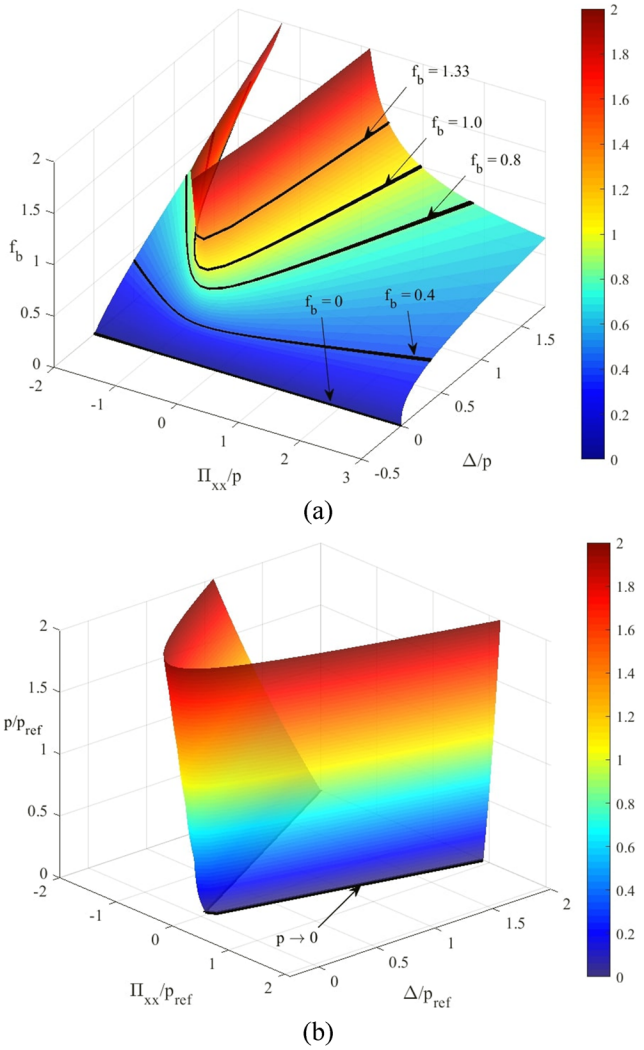

FIG. 5. Topology of the second-order Boltzmann–Curtiss-based constitutive models in the compression and expansion flow problem: (a) topology in a phase space (Π_{xx}/p, Δ/p, f_b) and (b) topology in a phase space (Π_{xx}/p_{ref}, Δ/p_{ref}, p/p_{ref}) for $f_b = 1.0$.

coupling factor $q_{2nd}(c\hat{R})$ and the driving force $\hat{\Pi}_{xx_0}$ are canceled out, leaving only a common kinematic viscous stress constraint between the xx-component of the shear stress and the excess normal stress,

$$9f_b\hat{\Pi}_{xx}^2 + \left(9f_b^2 - 4\right)\hat{\Pi}_{xx}\hat{\Delta} - 4f_b\hat{\Delta}^2 + 3f_b\hat{\Pi}_{xx} - \hat{\Delta} = 0$$

or

$$\hat{\Delta} = \frac{1}{8f_b}\left\{\left(9f_b^2 - 4\right)\hat{\Pi}_{xx} - 4 + \sqrt{\left(81f_b^4 + 72f_b^2 + 16\right)\hat{\Pi}_{xx}^2 + \left(32 - 24f_b^2\right)\hat{\Pi}_{xx} + 16}\right\}. \quad (34)$$

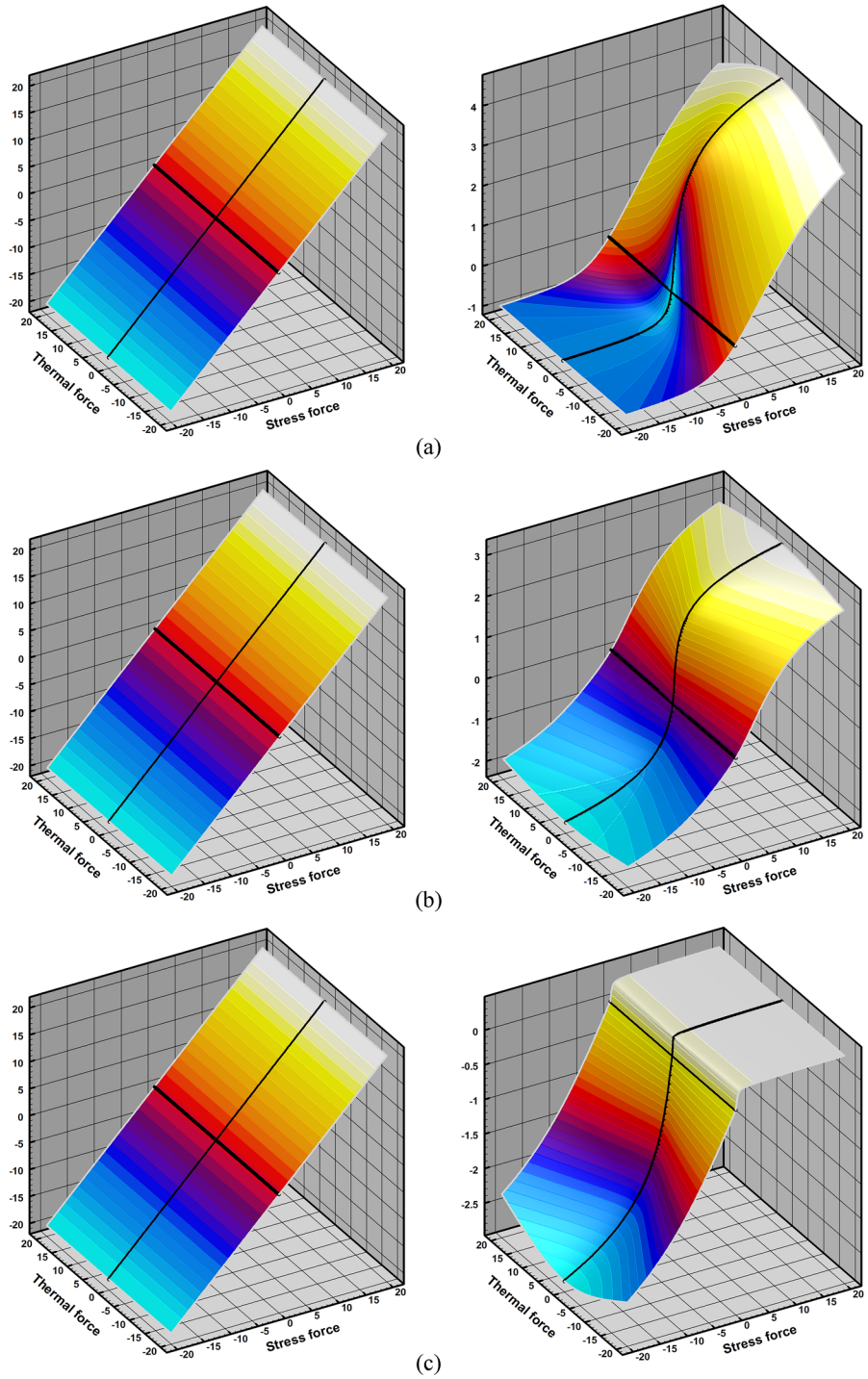

FIG. 6. Three-dimensional topology of viscous normal stress $\hat{\Pi}_{xx}$ for the first-order Navier–Fourier (left) and second-order Boltzmann–Curtiss-based (right) constitutive models for three values of f_b: (a) 0.0, (b) 0.8, and (c) f_b = 1000.

When the kinematic viscous stress constraint (34) is expressed using the following simple notation:

$$x \equiv \hat{\Pi}_{xx} = \frac{\Pi_{xx}}{p}, \quad y \equiv \hat{\Delta} = \frac{\Delta}{p},$$

the topology of the second-order constitutive model of compression and expansion is governed by *a conic section* expressed as a second-degree polynomial equation in the phase space (x, y),

$$9f_b x^2 + \left(9f_b^2 - 4\right)xy - 4f_b y^2 + 3f_b x - y = 0,$$

or

$$(9f_b x - 4y)(x + f_b y) + 3f_b x - y = 0$$

or

$$Ax^2 + Bxy + Cy^2 + Dx + Ey + F = 0,$$

where

$$A = 9f_b,\ B = 9f_b^2 - 4,\ C = -4f,\ D = 3f_b, E = -1,\ F = 0. \tag{35}$$

Then, determinants of the matrix of the quadratic form (A_{33}) and the conic section (A_Q) become, respectively,

$$\det A_{33} = -\frac{1}{4}(4 + 9f_b^2)^2,\ \det A_Q = \frac{3}{4}f_b\left(1 + 3f_b^2\right) \text{ with rank 3.} \tag{36}$$

In contrast to the velocity shear case, the present conic section is always a hyperbola, since the determinant of A_{33} is negative. The matrix representation of the present conic section is not degenerate, yielding a smooth topology with the derivatives of all orders everywhere. In addition, since the determinant of A_{33} is not zero, a geometric center of the hyperbola exists,

$$\begin{bmatrix} x_c \\ y_c \end{bmatrix} = \frac{1}{(4 + 9f_b^2)^2}\begin{bmatrix} -\left(4 + 15f_b^2\right) \\ -3f_b\left(2 + 9f_b^2\right) \end{bmatrix}. \tag{37}$$

Finally, the eccentricity of the present hyperbola can be written as

$$e = \frac{\sqrt{2}\sqrt[4]{81f_b^4 + 97f_b^2 + 16}}{\sqrt{5f_b + \sqrt{81f_b^4 + 97f_b^2 + 16}}}. \tag{38}$$

A topological representation of the second-order Boltzmann–Curtiss-based constitutive models (34) and (35) in the compression and expansion flow problem is given in a phase space (x, y, f_b) in Fig. 5(a). In contrast to the velocity shear case, the topology remains a hyperbola for all values of f_b. The eccentricity of the hyperbola varies from $\sqrt{2}$ ($f_b = 0$) to the lowest value of $\sqrt{13}/3$ ($f_b = \sqrt{2}/3$) and then asymptotically recovers the initial value of $\sqrt{2}$ ($f_b \to \infty$). The branch of compression obtained for positive x is almost linear, but the branch of expansion obtained for negative x is highly nonlinear and changes the sign of y.

The second-order Boltzmann–Curtiss-based constitutive model in the compression and expansion flow problem can be also represented in a different phase space (xp, yp, p)—equivalently, (Π_{xx}, Δ, p)—for a given value of f_b, as shown in Fig. 5(b). In the case of $f_b = 0$, it reduces simply to $y = 0$ or $\Delta = 0$. In the case of non-zero f_b, the topology remains a hyperbola for all values of p. In the limit of vanishing pressure, the hyperbola approaches the straight lines defined by $y = (9/4)f_b x$ in compression and $y = -x/f_b$ in expansion.

In order to further investigate the topology of the Boltzmann–Curtiss-based constitutive model for the relationship between the unknown stress and heat flux ($\hat{\Pi}_{xx}$, $\hat{\Delta}$, $\hat{Q}_x$) and the known driving (stress and thermal) forces of ($\hat{\Pi}_{xx_0}$, $\hat{Q}_{x_0}$), the second-order constitutive model (32) and (33) is solved numerically in terms of the driving forces $\hat{\Pi}_{xx_0}$, $\hat{Q}_{x_0}$ in conjunction with (34) by the method of iteration. The solutions of the second-order constitutive model for $\hat{\Pi}_{xx}$, $\hat{\Delta}$, $\hat{Q}_x$ are compared in Figs. 6–13. We considered three gases: monatomic argon ($f_b = 0$), diatomic nitrogen ($f_b = 0.8$), and linear polyatomic carbon dioxide ($f_b = 1000$). We excluded the polyatomic methane gas ($f_b = 1.33$), since it turned out that there was no significant difference with the diatomic nitrogen gas ($f_b = 0.8$).

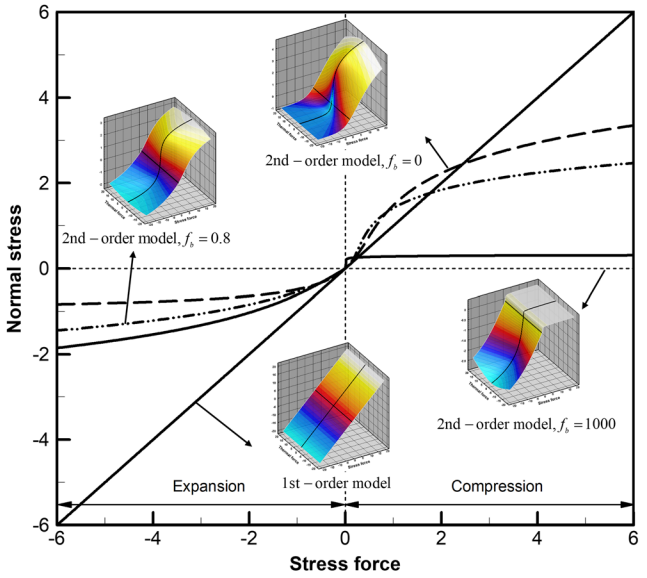

FIG. 7. A cross section of the topology of viscous normal stress $\hat{\Pi}_{xx}$ at the plane defined by zero thermal force for three values of f_b.

Figure 6 illustrates the three-dimensional topology of viscous normal stress $\hat{\Pi}_{xx}$ for the first-order Navier–Fourier and second-order Boltzmann–Curtiss-based constitutive models for three values of f_b. Note that topological representations of the first-order Navier–Fourier constitutive models are trivial, since the Navier–Fourier relations are linear, and therefore, they are nothing but $\mathbf{\Pi} \leftarrow \mathbf{\Pi}_0\ (\equiv -2\mu[\nabla \mathbf{u}]^{(2)})$, $\mathbf{Q} \leftarrow \mathbf{Q}_0 (\equiv -k\nabla T)$.

Figure 7 shows a cross section of the topology of viscous normal stress at the plane defined by $\hat{Q}_{x_0} = 0$ or zero thermal force. It is obvious that the topology of the first-order constitutive model to the driving (stress and thermal) forces is linear and has uncoupled stress and thermal components. The viscous stress is a function of the stress force but is independent of the thermal force.

On the other hand, the topology of the second-order Boltzmann–Curtiss-based constitutive model becomes highly nonlinear for all cases as the driving forces increase. In addition, the topology becomes strongly coupled to the stress and thermal components, as evidenced by the curved surface in the thermal force direction for a specified value of stress force. That is, the viscous stress varies nonlinearly with respect to the thermal force, although it is more influenced by the stress force. While the topologies of both models remain symmetric with respect to the plane defined by zero thermal force, the topology of the second-order model becomes

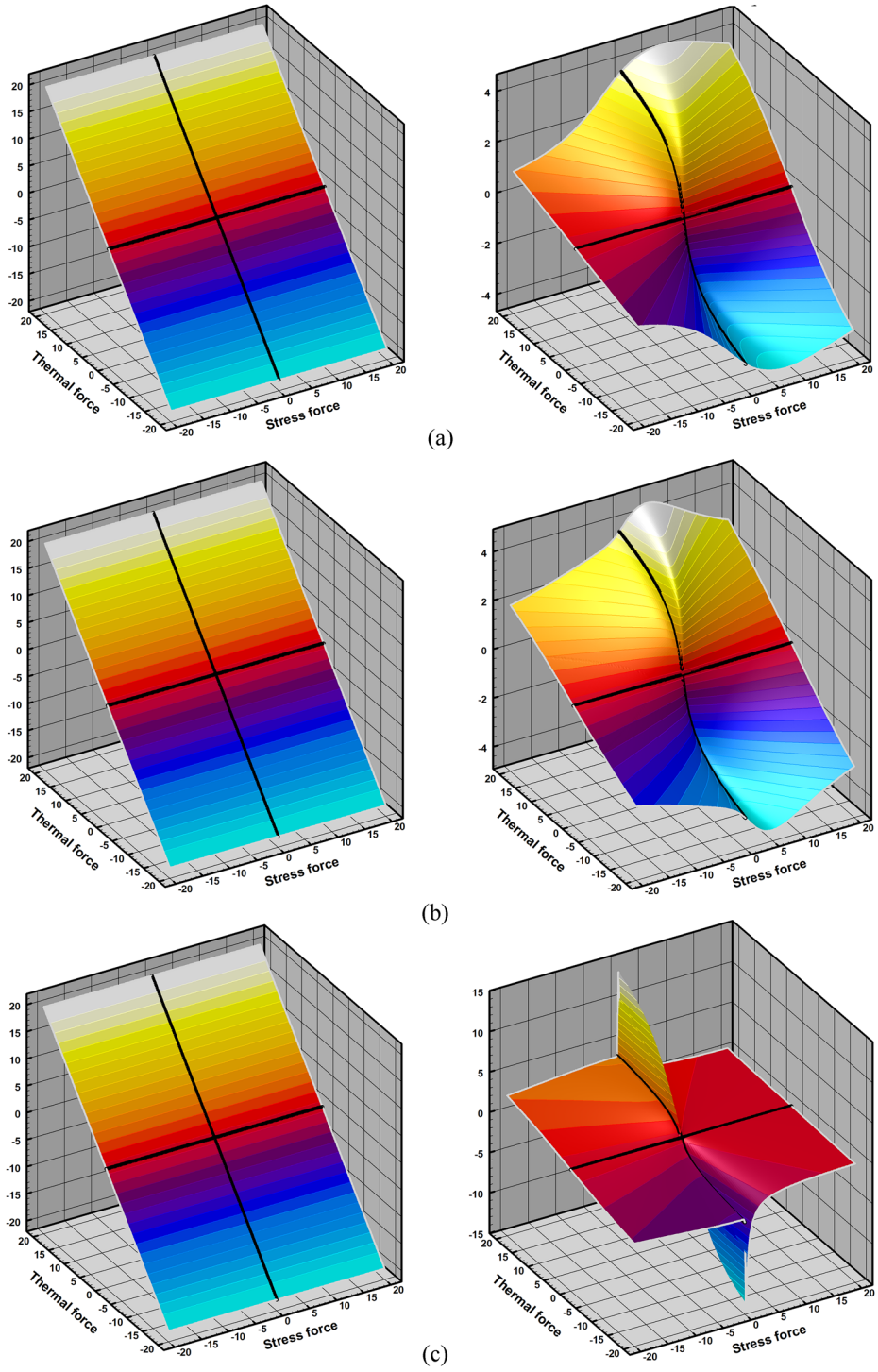

FIG. 8. Three-dimensional topology of heat flux $\hat{Q}_x$ for the first-order Navier–Fourier (left) and second-order Boltzmann–Curtiss-based (right) constitutive models for three values of f_b: (a) 0.0, (b) 0.8, and (c) 1000.

non-symmetric, resulting in a drastic difference in compression (positive stress force) and expansion (negative stress force) in gaseous states far from thermal non-equilibrium.

The ultimate origin of the nonlinear behavior can be traced to the second-order kinematic coupling term $\left(f_b\hat{\Delta}+\hat{\Pi}_{xx}\right)\hat{\Pi}_{xx_0}$ and the dissipative sinh (hyperbolic sine) nonlinear term $\hat{\Pi}_{xx}\,q_{2nd}(c\hat{R})$ in the second-order Boltzmann–Curtiss-based constitutive model in (32). It turns out that the second-order kinematic term plays a dominant role in expansion (negative stress force), while the second-order sinh dissipative term plays a critical role in compression

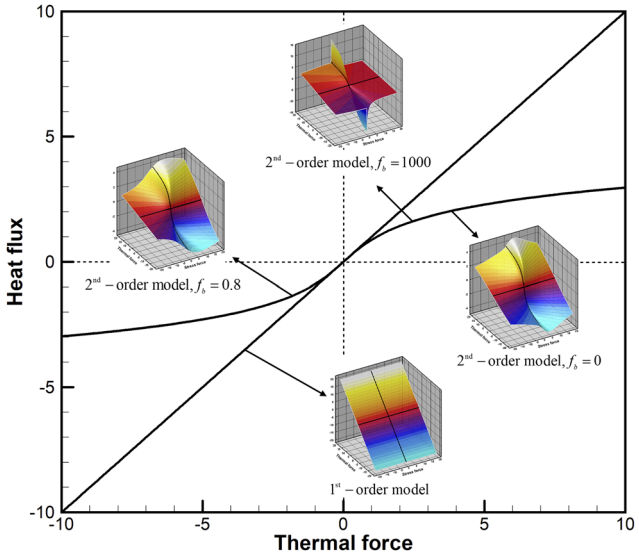

FIG. 9. A cross section of the topology of heat flux $\hat{Q}_x$ at the plane defined by zero stress force for three values of f_b.

(positive stress force). This property can be explained by examining the second-order constitutive model for zero thermal force, as shown in Fig. 7.

In compression and expansion cases, the constitutive model is simplified to $\sinh \hat{\Pi}_{xx} = \hat{\Pi}_{xx_0} + \hat{\Pi}_{xx}\hat{\Pi}_{xx_0}$ for a monatomic gas. It can be easily proved that the second-order kinematic coupling term $\hat{\Pi}_{xx}\hat{\Pi}_{xx_0}$ plays a critical role in the branch of expansion for $\hat{\Pi}_{xx_0} < 0$, while the second-order sinh dissipative term $\sinh \hat{\Pi}_{xx}$ plays a critical role in the branch of compression for $\hat{\Pi}_{xx_0} > 0$. In addition, it is straightforward to show that the solutions of the second-order constitutive model satisfy the free-molecular limit $\hat{\Pi}_{xx} + f_b\hat{\Delta} \to -1$ or $\Pi_{xx} + \Delta + p \to 0$ in the case of expansion. In contrast, for dissipation-dominated compression, the solutions show logarithmic ($\sinh^{-1}$) asymptotic behavior due to the term $\sinh \hat{\Pi}_{xx}$. Furthermore, the coupling of stress and thermal components is present through the Rayleigh–Onsager dissipation function $\hat{R}$, in which all stress and thermal components are added.

It can be also noted from Fig. 6(a) that, for a monatomic gas with $f_b = 0$, both stress and thermal forces contribute almost equally in the topology of the viscous stresses. On the other hand, as the value of f_b increases, the influence of thermal force on the topology decreases, while the influence of stress force increases due to the increasing contribution of excess normal stress, as shown in Fig. 6(b). At the extremely large value of $f_b = 1000$, the topology is dominated by the stress force, in particular, in the branch of compression (positive stress force), as shown in Fig. 6(c).

Figure 8 illustrates the topology of heat flux $\hat{Q}_x$ for the first-order Navier–Fourier and second-order Boltzmann–Curtiss-based constitutive models for three values of f_b. Figure 9 shows the cross section of the topology of heat flux at the plane defined by $\hat{\Pi}_{xx_0} = 0$ or zero thermal force. Again the topology of the first-order constitutive model to the driving (stress and thermal) forces is linear and uncoupled to the stress and thermal components. The heat flux is a function of the thermal force but is independent of the stress force. The topology of heat flux remains unchanged with increasing the f_b values.

On the other hand, the second-order constitutive model shows nonlinear behavior in both the stress and thermal forces. It can be observed from Fig. 8(a) that, for a monatomic gas with $f_b = 0$, the heat flux is more strongly affected by the thermal force than the stress force. As the bulk viscosity increases to $f_b = 0.8$, the influence of the stress force decreases and the heat flux exhibits asymmetric behavior with respect to the plane defined by zero stress force. Eventually, the heat flux shows a fully asymmetric topology and takes the shape of a shark fin at the extremely large value of $f_b = 1000$, as shown in Fig. 8(c). Such asymmetry can be explained by examining the constitutive model for zero stress force, which is simplified into $\hat{Q}_x = \frac{1}{c}\sinh^{-1}(c\hat{Q}_{x_0})$ for all values of f_b, as shown in Fig. 9.

Figure 10 highlights the topology of excess normal stress $\hat{\Delta}$ for the first-order and second-order Boltzmann–Curtiss-based constitutive models. Figure 11 shows the cross section of the topology of excess normal stress at the plane defined by $\hat{Q}_{x_0} = 0$ or zero thermal force. It should be noted that the topology of excess normal stress $\hat{\Delta}$ is directly connected to the topology of normal stress $\hat{\Pi}_{xx}$ via the hyperbolic topology of the second-order Boltzmann–Curtiss-based constitutive model (34) and (35), as illustrated in Fig. 5. In a monatomic gas with $f_b = 0$, excess normal stress does not play any role, as shown in Fig. 10(a). When the value of f_b increases, the excess normal stress in the first-order model shows a linear behavior similar to the normal stress shown in Fig. 6.

On the other hand, the second-order constitutive model exhibits a strong nonlinear feature, in particular, in the stress force, as shown in Figs. 10(b) and Fig. 11. When the value of f_b increases to 1000, the influence of the thermal force vanishes, as shown in Fig. 10(c).

Figure 12 shows the topology of the Rayleigh–Onsager dissipation function $\hat{R}$ for the first-order and second-order Boltzmann–Curtiss-based constitutive models. Figure 13 shows the cross section of the topology of the dissipation function at the plane defined by zero thermal force.

The function $\hat{R}$ defined in (20) can be also regarded as a non-equilibrium parameter, since it is directly proportional to the parameter N_δ that measures the degree of non-equilibrium. In the first-order constitutive model, the dissipation function has a circular shape at the small values of f_b, which implies that there is uniform contribution by the stress and thermal forces in all directions. In contrast, the dissipation function of the second-order constitutive model is not equally distributed and such non-uniformity increases with increasing value of f_b. In fact, it can be noted from Fig. 12(c) that the dissipation function becomes dominated by the stress force at the extremely large value of $f_b = 1000$, as evidenced by the vanishing role of the thermal force in states far from thermal non-equilibrium.

IV. TRAJECTORY OF THE SHOCK STRUCTURE SOLUTION ON THE TOPOLOGY OF THE SECOND-ORDER BOLTZMANN–CURTISS BASED CONSTITUTIVE MODEL

A. Compressive shock structure

A shock structure with strong gradients is regarded as one of the fundamental problems in the kinetic theory of gases and has been studied by many theoreticians and experimentalists for the

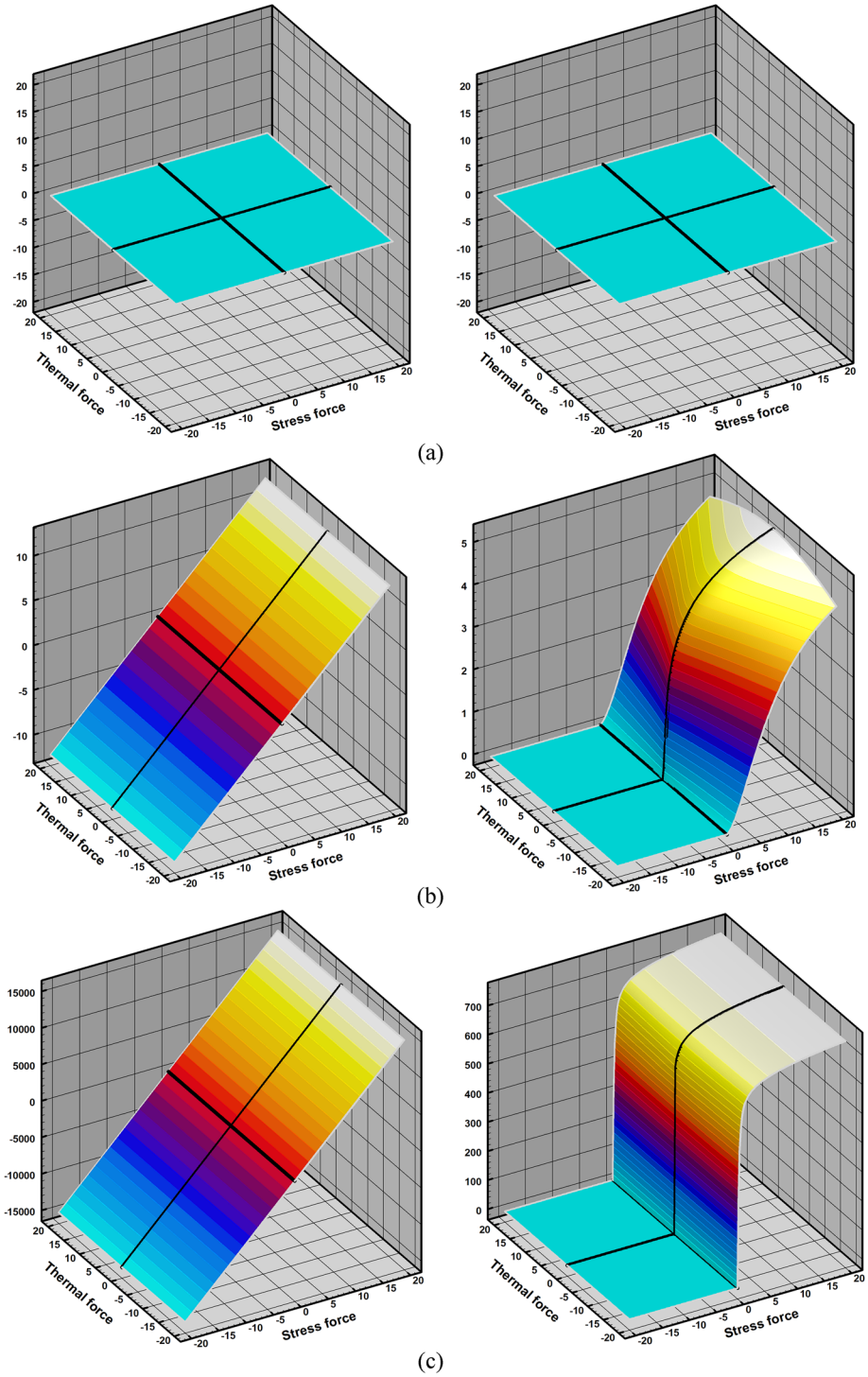

FIG. 10. Three-dimensional topology of excess normal stress $\hat{\Delta}$ for the first-order Navier–Fourier (left) and second-order Boltzmann–Curtiss-based (right) constitutive models for three values of f_b: (a) 0.0, (b) 0.8, and (c) 1000.

several decades.[19–21,46,61,72–77] For example, it has a big impact on the overall flow patterns around hypersonic aerospace vehicles at high altitude.[78] Although the shock structure problem does not involve any solid boundary, the calculation of the shock structure presents severe theoretical and computational challenges. For instance, the high order hydrodynamic approach based on the Grad's moment method failed to yield shock solutions beyond a relatively small value of M ($\doteq$1.65).[73]

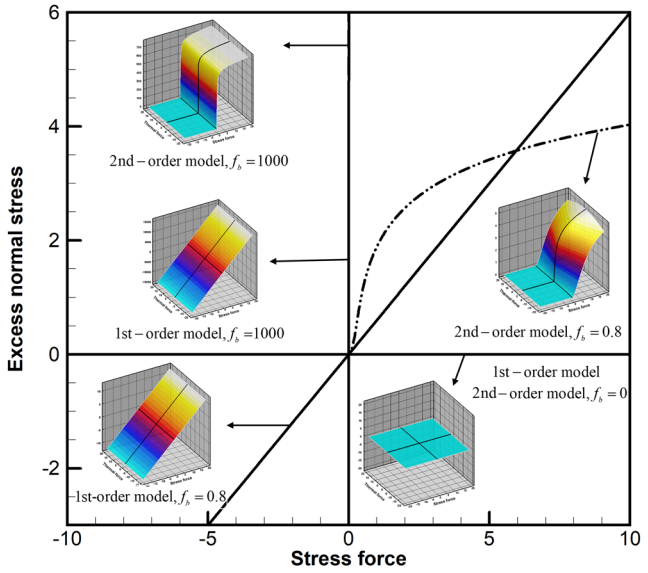

FIG. 11. A cross section of the topology of excess normal stress $\hat{\Delta}$ at the plane defined by zero thermal force for three values of f_b.

The stationary shock wave structure problem is defined as a very thin (on the order of the mean free path, in other words, a Knudsen number close to 1.0) stationary gas flow region between the supersonic upstream and subsonic downstream. The upstream and downstream states are determined by the so-called Rankine–Hugoniot condition.[19] For a comparison of various results of the shock structure, the following parameters can be very useful: the inverse of the shock density thickness (δ^{-1}) and the shock temperature-density separation (Δ_s), which measures the separation between density and temperature profiles, defined as

$$\delta^{-1} = \frac{1}{\left(\bar{\rho}_2 - \bar{\rho}_1\right)}\left|\frac{d\bar{\rho}}{dx}\right|_{\max}, \quad \Delta_s = \left[x(\bar{\rho} = 0.5) - x\left(\bar{T} = 0.5\right)\right], \quad (39)$$

where the subscripts 1 and 2 denote the upstream and downstream states, and $\bar{\rho}$ and $\bar{T}$ are the normalized density and temperature profiles defined as

$$\bar{\rho} = \frac{\rho - \rho_1}{\rho_2 - \rho_1}, \quad \bar{T} = \frac{T - T_1}{T_2 - T_1}. \quad (40)$$

In addition, for the known density profile, the shock asymmetry (Q_s) can be expressed as follows:

$$Q_s = \frac{\int_{-\infty}^{0}(\rho(x) - \rho_1)dx}{\int_{0}^{\infty}(\rho_2 - \rho(x))dx} = \frac{\int_{\rho_a}^{\rho_1} x(\rho)d\rho}{\int_{\rho_a}^{\rho_2} x(\rho)d\rho}. \quad (41)$$

Note that the area defined by the integration $\int_0^\infty (\rho_2 - \rho(x))dx$ is equal to the area defined by the integration $\int_{\rho_a}^{\rho_2} x(\rho)d\rho$ in the present monotonic shock profile bounded by ρ_1 and ρ_2. The density ρ_a at the central position $x = 0$ is defined as the arithmetic mean of the upstream and downstream density. In the numerical results, we use x/λ as a spatial variable, which was non-dimensionalized by the mean free path $\lambda = \sqrt{(\pi/2RT)}\mu/\rho$.

B. Numerical method based on an explicit modal discontinuous Galerkin method and its validation

The conservation laws (10) in conjunction with zero-order, first-order, and second-order constitutive models, described in (13), (14) and (18), (20), respectively, were solved by the one-dimensional explicit modal discontinuous Galerkin (DG) method.[79,80] The domain was decomposed into line elements, and the scaled Legendre basis functions were employed for elements. The Gauss–Legendre quadrature rule was implemented for both the volume and the boundary integrations, and Roe's flux was applied for the inviscid terms, while the BR1 scheme[81] was employed for the auxiliary and viscous fluxes at the elemental interfaces. A polynomial expansion of third-order accuracy was used to approximate solutions in the finite element space, and the third-order total variation diminishing Runge–Kutta (TVD-RK) scheme was used for time integration. To eliminate the spurious numerical fluctuations of the solutions, the Hermite weighted essentially non-oscillatory (WENO) limiter proposed by Cockburn and Shu[82] was used.

In order to validate the present computational model and associated numerical DG solver, we compared the solutions of the inverse shock density thickness—one of the important factors characterizing the shock structure—obtained from the first-order and second-order models and experimental data for monatomic argon and diatomic nitrogen gases.[83–86]

Figure 14 shows that the general configuration of the shock inverse density thickness for the second-order Boltzmann–Curtiss based model is in excellent agreement with the experimental data. The second-order Boltzmann–Curtiss based model precisely captured the shock-density thickness for all Mach number regimes. The numerical results show that the first-order model yields an inverse shock density thickness that is much larger than the experimental data.

Figure 15 compares the normalized density solutions of the shock structure in nitrogen gas for various Mach numbers (1.53, 3.0, 6.1, and 10) with the experimental data.[83] It shows that the difference between the first-order solution and experimental data becomes noticeable for high Mach number flows, while the second-order solution is very close to the experimental data.

C. Connection between sinh-dominated topology and shock structure solution

The existence of a topology in the kinematic stress constraints and the relationship between the non-conserved properties and the thermodynamic forces in the constitutive model implies that, when the diatomic and polyatomic gases with a specific value of f_b undergo compression, the non-conserved variables appearing in the conservation laws must be determined on the surface of sinh-dominated topology and hyperbola in the phase space. In the case of velocity shear, the second-order solutions were taken from previous analytical studies on a force-driven Poiseuille gas flow.[50,68] Therefore, it will be instructive to investigate the connection between the topology and a flow solution by computing the trajectories of the shock structure solution on the topology of the second-order constitutive model. For this purpose, we consider the shock structure problem of Mach numbers 3 and 5 in monatomic ($f_b = 0$) and diatomic ($f_b = 0.8$) gases.

Figure 16 illustrates the connection between the topology of viscous normal stress and the shock structure solution in monatomic

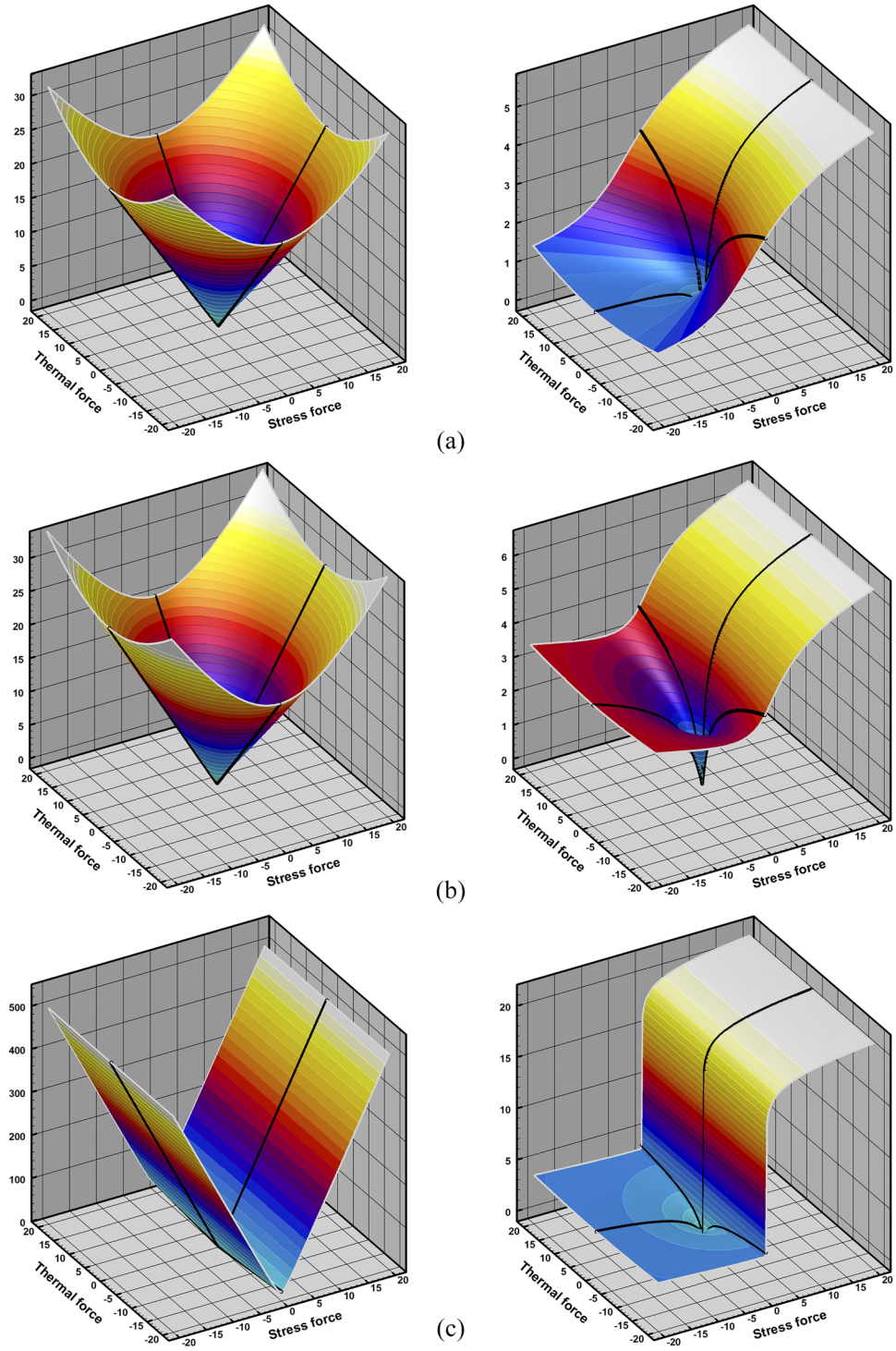

FIG. 12. Three-dimensional topology of the dissipation function $\hat{R}$ for the first-order Navier–Fourier (left) and second-order Boltzmann–Curtiss-based (right) constitutive models for three values of f_b: (a) 0.0, (b) 0.8, and (c) 1000.

and diatomic gases. In Fig. 16, the origin (0,0) denotes the equilibrium solutions of the shock structure, that is, upstream and downstream. Note that the trajectories are located in the fourth quadrant defined by positive stress and negative thermal forces. The shape of the trajectories was found to remain the same in the following sense: (1) it is a not-overlapped, not-crossing topology, and (2) the upstream branch is closer to the zero thermal force curves than the downstream branch. On the other hand, the range of trajectories

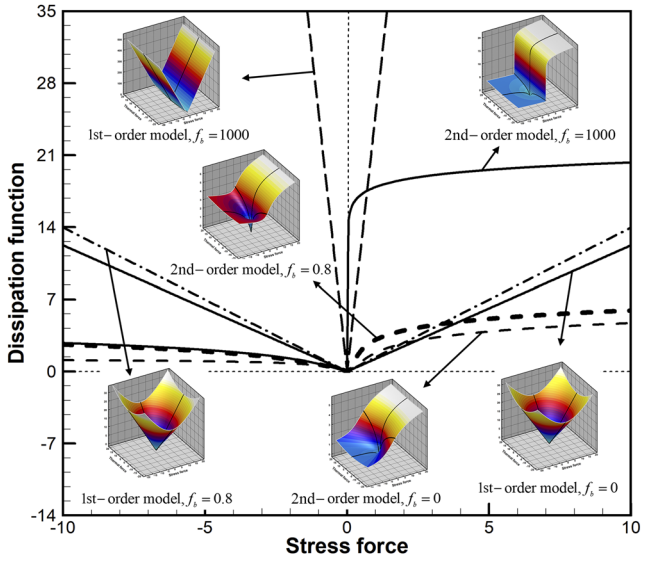

FIG. 13. A cross section of the topology of the dissipation function $\hat{R}$ at the plane defined by zero thermal force for three values of f_b.

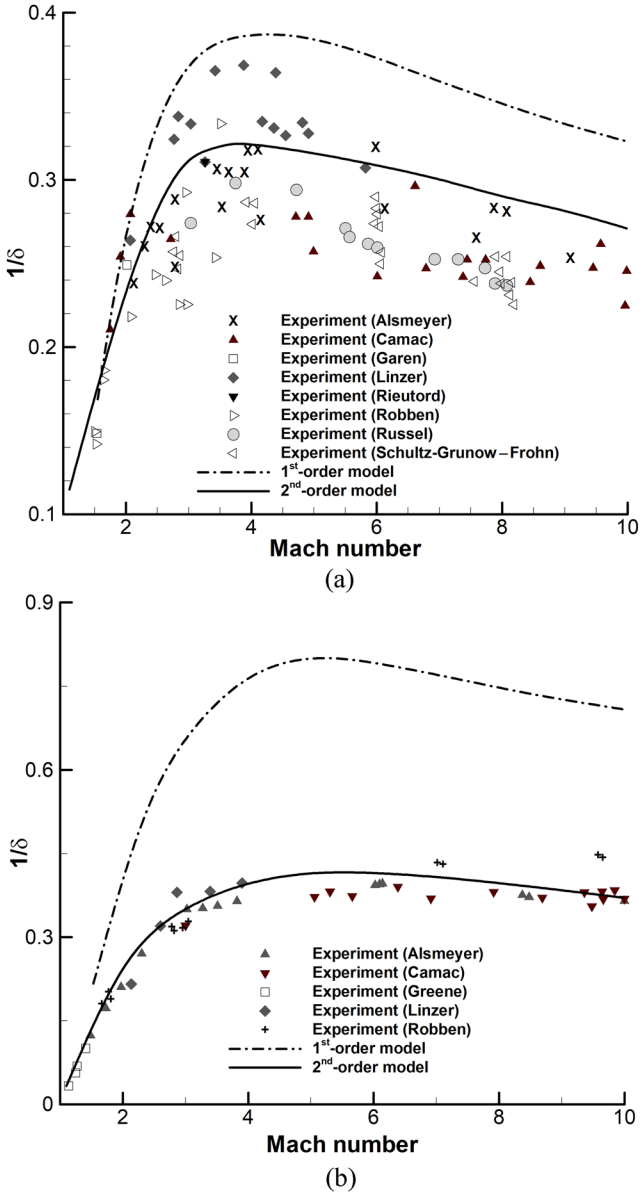

FIG. 14. Inverse density thickness of the shock wave structure: (a) argon and (b) nitrogen.

from the origin changes substantially with respect to the values of f_b and Mach number. In particular, the range increases with increasing Mach number, since the Mach number contributes directly to thermal non-equilibrium.

Figure 17 illustrates the connection between the topology of heat flux and the shock structure solution in monatomic and diatomic gases. Like the normal stress case, the trajectories on the topology are not-overlapped, not-crossing, and the upstream branch is closer to the zero stress force curve than the downstream branch. The range of trajectories from the origin also increases with increasing Mach number. Figure 18 illustrates the connection between the topology of the dissipation function and the shock structure solution in monatomic and diatomic gases. As expected, the trajectories are located in the fourth quadrant and are not overlapped.

D. Effects of diatomic and polyatomic gases on the shock structure

We investigated the effects of diatomic and polyatomic gases on the shock structure solutions: profiles, topology in phase space, and the main characteristics. For this purpose, we selected three gases: monatomic argon (f_b = 0), diatomic nitrogen (f_b = 0.8), and linear polyatomic methane (f_b = 1.33). Figure 19 summarizes the effects of diatomic and polyatomic gases on the shock structure at Mach = 3.0: the conserved variables (density, velocity and temperature), the non-conserved variables (stress and heat flux), the stress vs heat flux in the phase space, and the dissipation function.

An interesting feature is that the shock transition regime extends upstream as the value of f_b increases, as shown in Figs. 19(a)–19(b). There is a noticeable difference in the trajectories of the shock solutions in the phase space of the viscous stress and heat flux, as shown in Fig. 19(c). The effects of diatomic and polyatomic gases on the dissipation function ($\hat{R}$) are illustrated in Fig. 19(d). The shock transition regime follows nonlinear curves very different from the first-order dissipation function. The actual trend in the dissipation function is very similar to the topological cross-sectional plot depicted in Fig. 13.

Finally, we investigated the effects of diatomic and polyatomic gases on the main characteristics of shock structure—inverse density thickness, asymmetry, and temperature–density separation distance. In order to examine the effect of the order of the constitutive model,

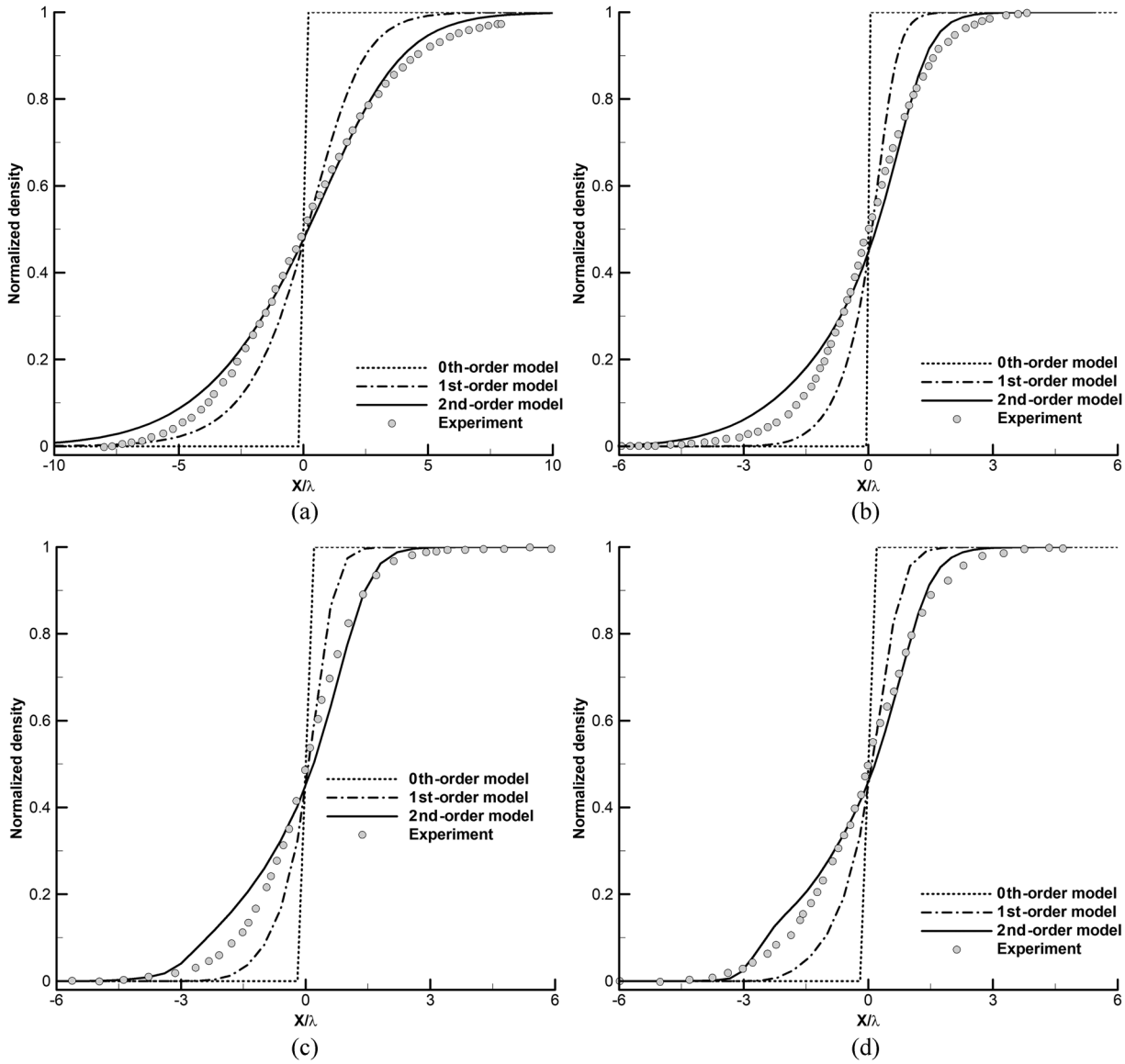

FIG. 15. Comparison of normalized density solutions of 0th-, 1st-, and 2nd-order models for nitrogen gas in the shock structure problem for various Mach numbers: (a) 1.53, (b) 3.8, (c) 6.1, and (d) Mach = 10.0.

the first-order NSF analytical solutions are also considered. Full analytical NSF solutions in closed elementary functional form in the case of Pr = 3/4 were developed in 2014 by Myong[72] for Maxwell and hard sphere molecules; for a Maxwellian molecule, the solutions of the implicit type are for dimensionless density r,

$$3\theta_1 M\sqrt{\frac{\gamma\pi}{2}}\frac{x}{\lambda} = \frac{1}{r_a}\left(\frac{5}{4}+\frac{1}{2r_a}\right) - \frac{1}{r}\left(\frac{5}{4}+\frac{1}{2r}\right) + \frac{4}{\chi}\ln\frac{\left[(r_1^{-1}-r^{-1})/(r_1^{-1}-r_a^{-1})\right]^{(2\varsigma-r_1^{-2})/r_1}}{\left[(r^{-1}-r_2^{-1})/(r_a^{-1}-r_2^{-1})\right]^{(2\varsigma-r_2^{-2})/r_2}}, \quad (42)$$

where

$$r_{1,2} = \rho_1 O^{-2} P = \frac{1}{v_{1,2}} = \frac{8}{5\pm\chi},\ r_a = \frac{1}{2}(r_1+r_2) = \frac{5}{4\zeta},$$

$$\theta_{1,2} = \frac{15\mp 2\chi-\chi^2}{64},\ \chi = \sqrt{25-32\zeta},$$

$$\zeta = \frac{\gamma^2 M^2\left[2+(\gamma-1)M^2\right]}{2(\gamma-1)(1+\gamma M^2)^2},$$

and O, P are integration constants for the conservation laws of mass and momentum, respectively.

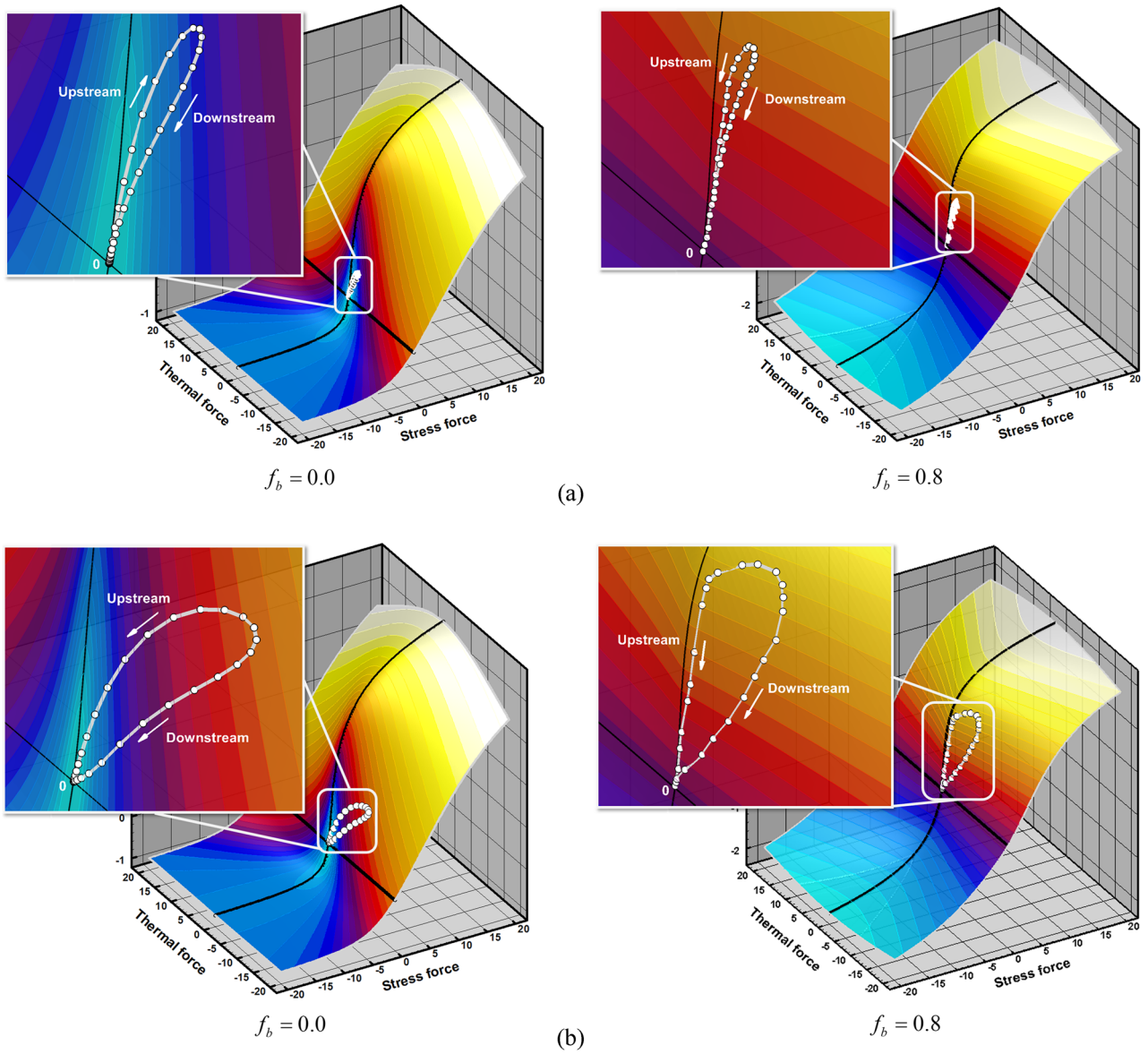

FIG. 16. Trajectories of the shock structure solution on the topology of viscous normal stress $\hat{\Pi}_{xx}$ in monatomic (left) and diatomic (right) gases: (a) Mach = 3.0 and (b) Mach = 5.0.

The shock thickness based on the maximum slope of the density in the shock profile can be computed by solving the following differential equation (s being the exponent of the inverse power laws of gas molecules):

$$\frac{dr}{d\xi} = \frac{3}{5}(5\theta_1)^s \frac{r(r-r_1)(r_2-r)}{r_1 r_2 (2\zeta - r^{-2})^s}, \text{ where } \xi = \sqrt{\frac{\gamma\pi}{2}} M \frac{x}{\lambda}. \tag{43}$$

However, by noting that $dr/d\xi$ becomes maximum at the location ξ satisfying

$$6\zeta^2 r^4 - 10\zeta r^3 + \zeta(1-2s)r^2 + 5(s+1)r - 2(2s+1) = 0, \tag{44}$$

the maximum slope can be determined without actually solving (43). A unique real root of the quartic equation of r ($r_1 < r < r_2$) can always be obtained using Ferrari's method.[87] The inverse shock density thickness δ is then calculated by

$$\delta^{-1} = \sqrt{\frac{\gamma\pi}{2}} \frac{M}{r_2 - r_1} \left(\frac{dr}{d\xi}\right)_{\max}.$$

On the other hand, for the known density profile, the shock asymmetry is reduced to[72]

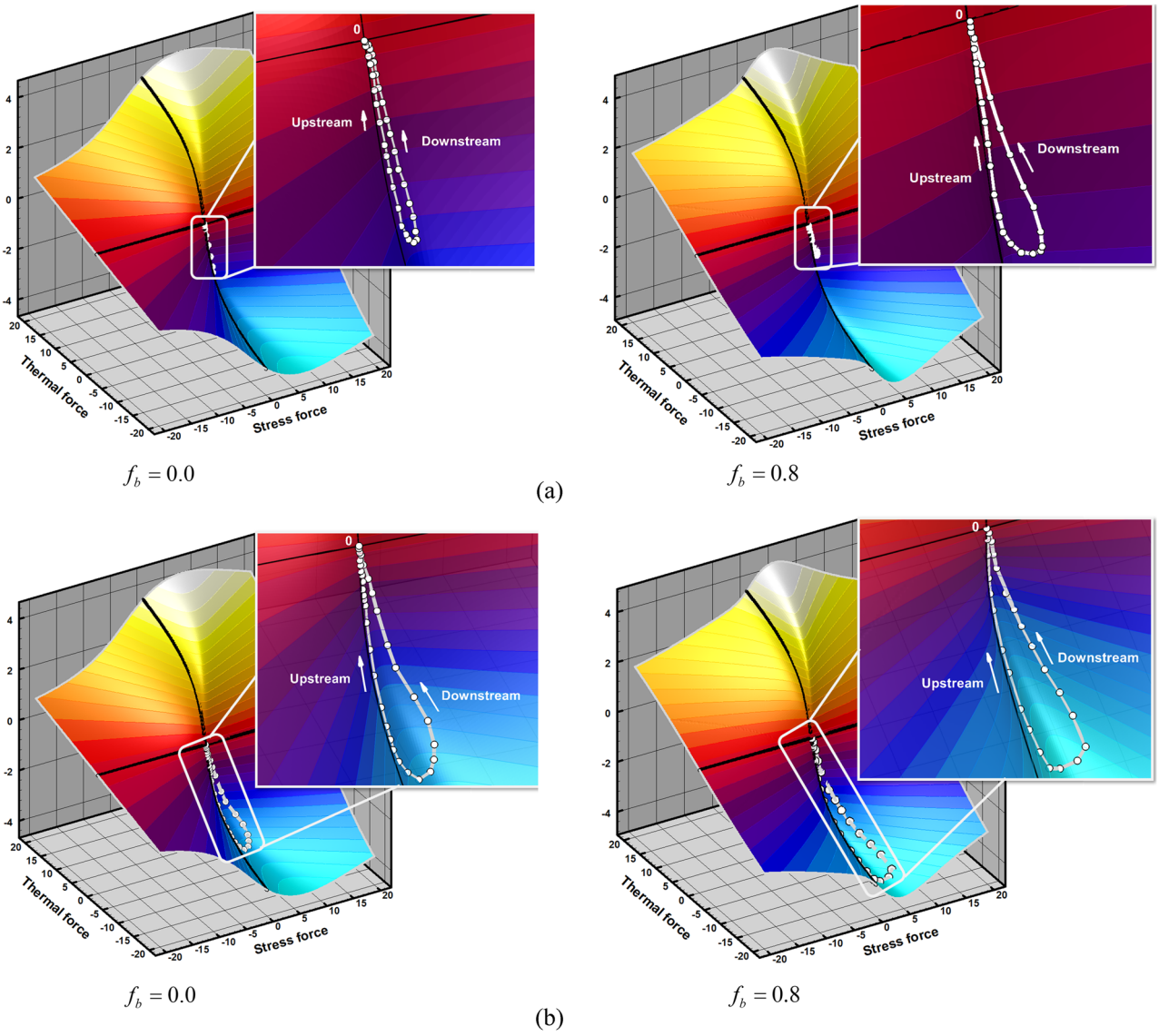

FIG. 17. Trajectories of the shock structure solution on the topology of heat flux $\hat{Q}_x$ in monatomic (left) and diatomic (right) gases: (a) Mach = 3.0 and (b) Mach = 5.0.

$$\frac{-\frac{\chi}{4}\left[\frac{5}{4}\ln\frac{r_1}{r_a}-\frac{1}{2}\left(\frac{1}{r_1}-\frac{1}{r_a}\right)-\frac{1}{r_a}\left(\frac{5}{4}+\frac{1}{2r_a}\right)(r_1-r_a)\right]-\frac{5}{4}\left(\frac{1}{r_2}-\frac{1}{r_1}\right)\ln\frac{r_1}{r_a}-\left(2\zeta-\frac{1}{r_2^2}\right)\left(1-\frac{r_1}{r_2}\right)\ln\left(\frac{r_a^{-1}-r_2^{-1}}{r_1^{-1}-r_2^{-1}}\right)}{-\frac{\chi}{4}\left[\frac{5}{4}\ln\frac{r_2}{r_a}-\frac{1}{2}\left(\frac{1}{r_2}-\frac{1}{r_a}\right)-\frac{1}{r_a}\left(\frac{5}{4}+\frac{1}{2r_a}\right)(r_2-r_a)\right]-\frac{5}{4}\left(\frac{1}{r_2}-\frac{1}{r_1}\right)\ln\frac{r_2}{r_a}-\left(2\zeta-\frac{1}{r_1^2}\right)\left(\frac{r_2}{r_1}-1\right)\ln\left(\frac{r_1^{-1}-r_a^{-1}}{r_1^{-1}-r_2^{-1}}\right)}. \tag{45}$$

Another parameter, the so-called shock temperature–density separation, can be easily calculated as follows:

$$\bar{x}(r_a)-\bar{x}(r(\theta_a)) = -\bar{x}(r(\theta_a))$$

where

$$r(\theta_a)=\left(\frac{32}{25-16\zeta}\right)^{1/2} \text{ and } \theta_a=\frac{\theta_1+\theta_2}{2}. \tag{46}$$

Figures 20–22 show the effects of diatomic and polyatomic gases on the important parameters of the shock wave structure

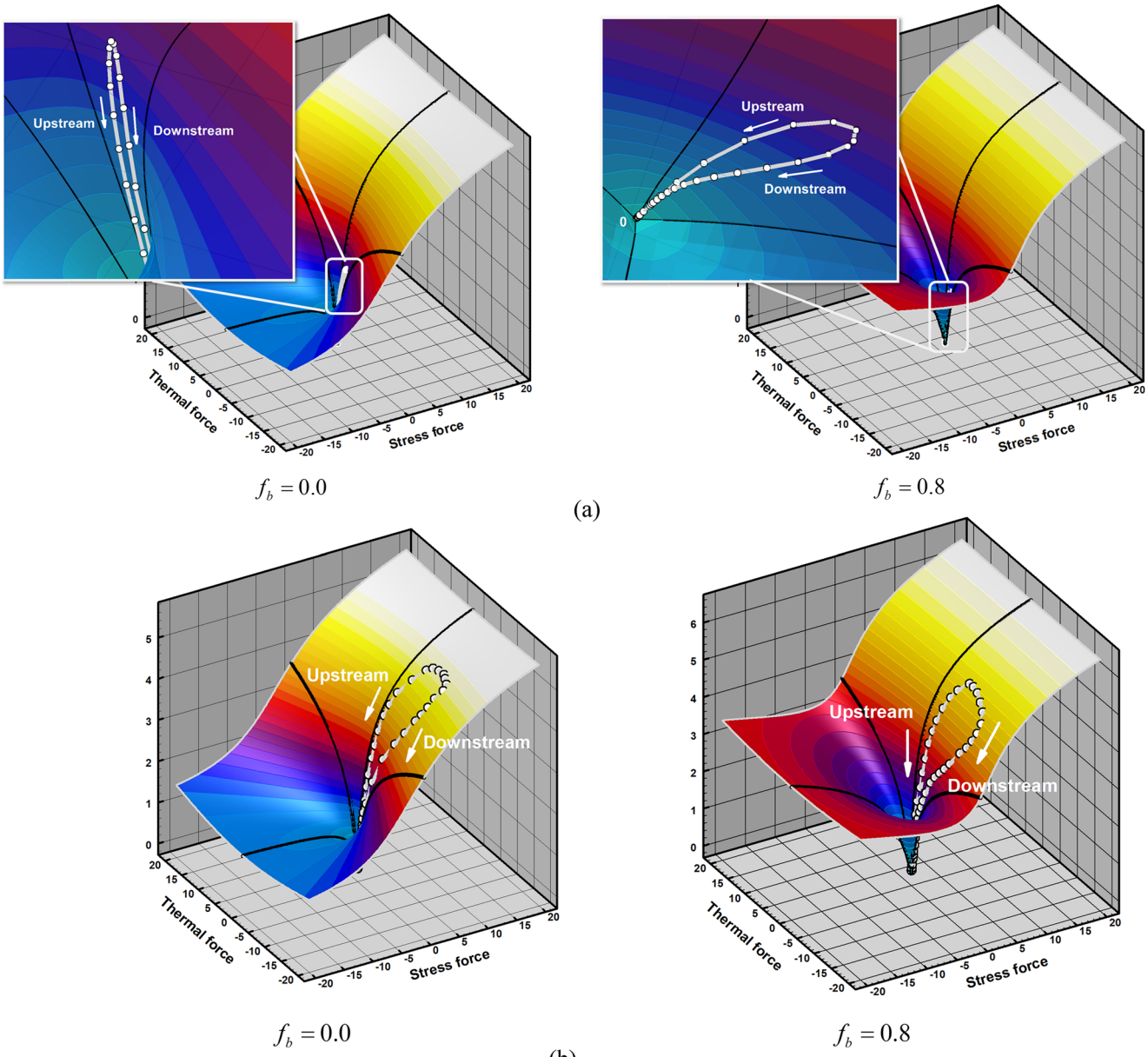

FIG. 18. Trajectories of the shock structure solution on the topology of the dissipation function $\hat{R}$ in monatomic (left) and diatomic (right) gases: (a) Mach = 3.0 and (b) Mach = 5.0.

for varying Mach numbers: the inverse density thickness, the asymmetry, and the temperature–density separation distance, respectively. The shock inverse density thickness is known as one of the more important parameters for characterizing the shock structure.

Figure 20 shows the inverse density thickness of three gases (monatomic argon, diatomic nitrogen, and linear polyatomic methane) computed by the second-order Boltzmann–Curtiss-based model. The full analytical NSF solution for a Maxwellian molecule ($s = 1$) is also shown for reference. All models show the same qualitative trend in the inverse density thickness—increase up to a critical Mach number and then decrease. However, the inverse density thickness increases with increasing f_b. The gap between argon and the Maxwellian molecule in a monatomic gas is due to the difference in the order of the constitutive model, the second-order and the first-order, respectively.

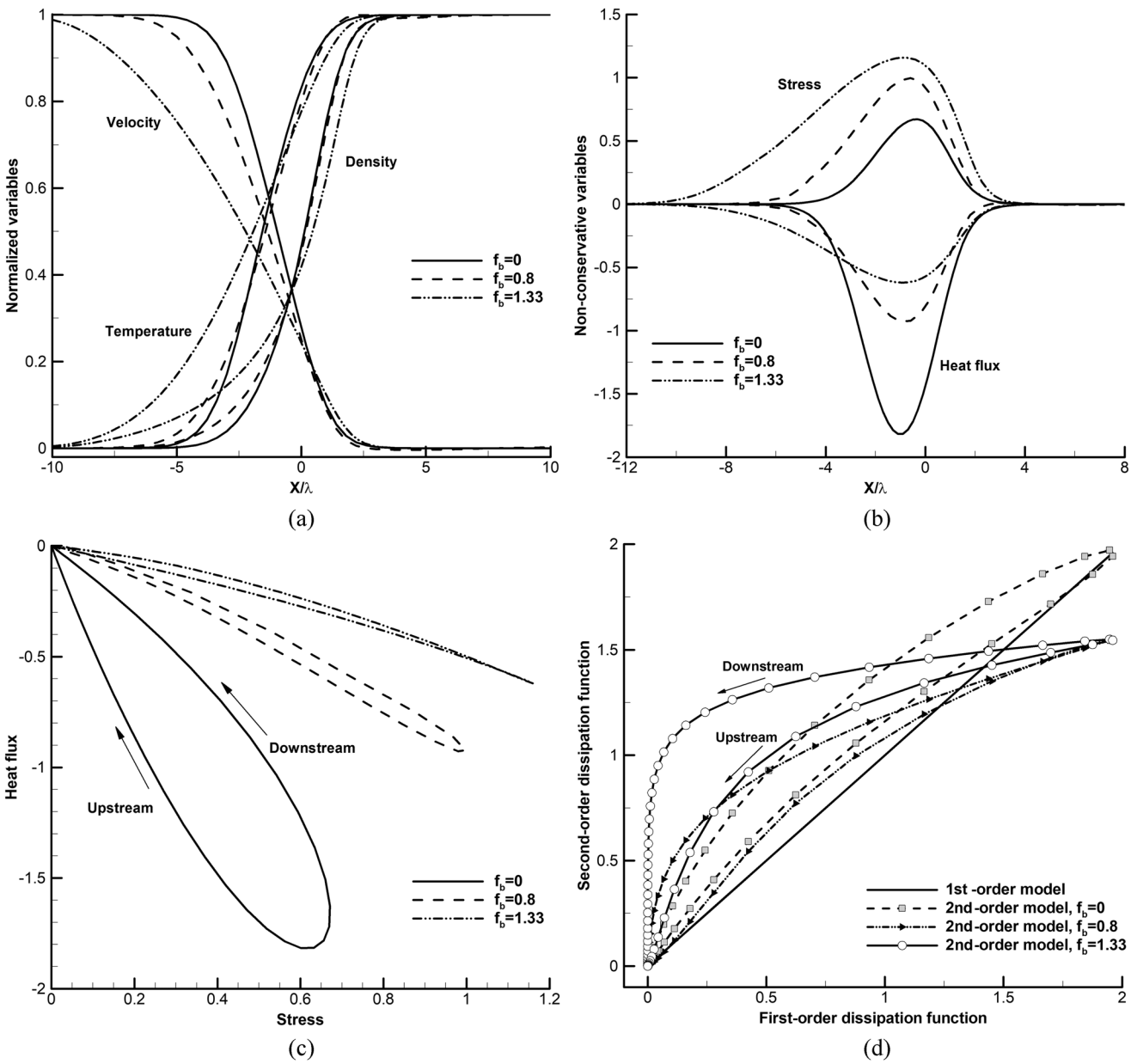

FIG. 19. Effects of diatomic and polyatomic gases on the shock structure at Mach = 3.0: (a) normalized conserved variables, (b) normalized non-conserved variables, (c) stress vs heat flux, and (d) 1st-order dissipation function vs 2nd-order dissipation function.

Figure 21 shows the asymmetry in the shock structure of the three gases. All gases exhibit an asymmetry bigger than 1, meaning that the upstream area is always bigger than the downstream area. All gases also show the same qualitative trend with increasing Mach number—a rapid increase and then approaching an asymptotic value. The asymptotic value of the asymmetry increases with increasing f_b. The first-order NSF model of the Maxwellian molecule shows the smallest asymmetry.

Figure 22 shows the temperature–density separation distance, another important parameter of the shock wave structure. All models show the same qualitative trend in the distance—a decrease up to a critical Mach number and then continuous increase. The temperature–density separation distance decreases with increasing f_b for all Mach numbers.

However, the most striking finding in Fig. 22 is the big gap between argon (second-order) and the Maxwellian molecule

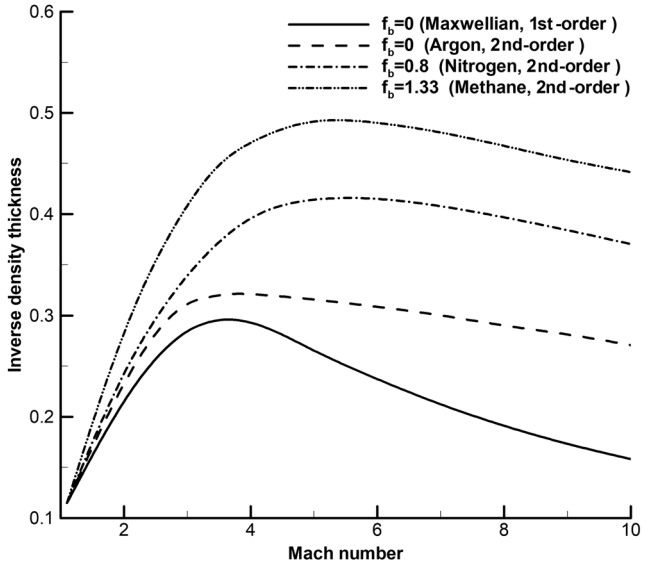

FIG. 20. Effects of diatomic and polyatomic gases on the inverse density thickness of the shock wave structure for varying Mach numbers (1st-order and 2nd-order Boltzmann–Curtiss solutions).

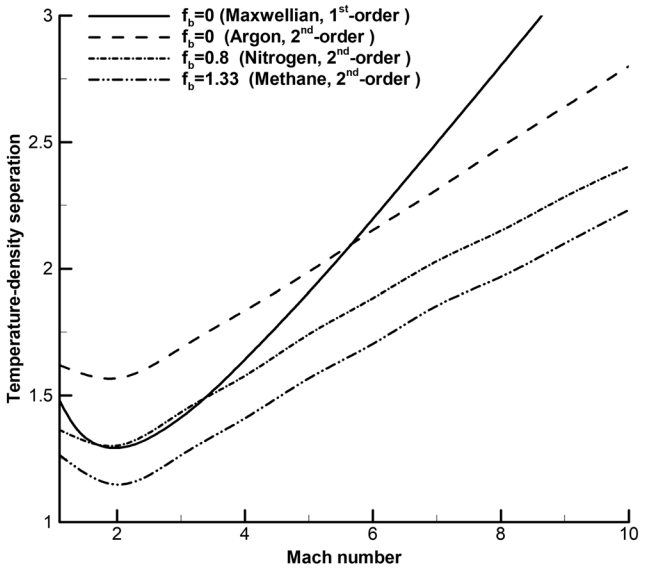

FIG. 22. Effects of diatomic and polyatomic gases on the temperature–density separation distance of the shock wave structure for varying Mach numbers (1st-order and 2nd-order Boltzmann–Curtiss solutions).

(first-order) in a monatomic gas. This difference implies that the effect of the order of the constitutive model on the shock structure is primarily highlighted by the temperature–density separation distance. In summary, it may be concluded that the bulk viscosity and the order of the constitutive model play essential roles in the non-equilibrium behavior of diatomic and polyatomic gases and, in particular, in the shock wave structure.

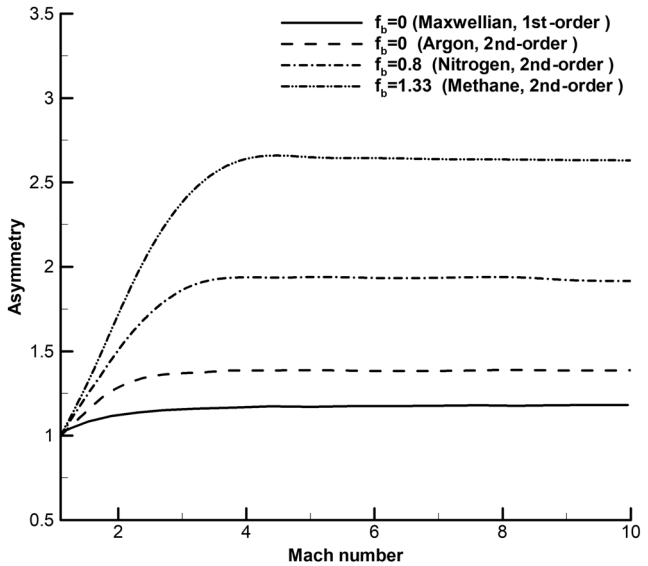

FIG. 21. Effects of diatomic and polyatomic gases on the asymmetry of the shock wave structure for varying Mach numbers (1st-order and 2nd-order Boltzmann–Curtiss solutions).

V. CONCLUDING REMARKS

The topological aspects of fluid flows have been fascinating subjects in studies on the physics of fluids. In this study, the topology of the second-order constitutive model beyond the conventional first-order NSF equations and Stokes's hypothesis was extensively investigated. The emphasis was placed on the general structure of the topology and the effects of thermal non-equilibrium and the bulk viscosity associated with the viscous excess normal stress on diatomic and polyatomic gases and their interplay in the topological space.

The second-order constitutive model was derived from the Boltzmann–Curtiss kinetic equation for diatomic and polyatomic molecules with a moment of inertia and an angular momentum. During the derivation, two tenets—the closing-last balanced closure and the cumulant expansion based on the canonical distribution function in the exponential form—were applied to the moment equations of the Boltzmann–Curtiss kinetic equation. The initial topology of the constitutive model in nine-dimensional phase space was decomposed into two subsets: the velocity shear and the compression and expansion.

In the case of velocity shear, the topology of the second-order constitutive model was shown to be governed by a conic section expressed as a second-degree polynomial equation in the phase space. The topology turned out to be always smooth, having the derivatives of all orders everywhere in its conic section. The bulk viscosity ratio in diatomic and polyatomic gases was found to play an essential role in determining the types of topology of the conic section: from an ellipse to a circle, to a parabola, and then finally to a hyperbola, with increasing bulk viscosity ratio. The ultimate origin

of the existence of the conic section and the rich topology of various conic sections was traced to the second-order coupling of the viscous stress and the velocity gradient of a kinematic nature and its subtle interplay with the bulk viscosity ratio in the second-order Boltzmann–Curtiss constitutive model. In the case of compression and expansion, the topology of the second-order constitutive model was also found to be governed by a conic section, but it was always a hyperbola, irrespective of the bulk viscosity ratio.

The topology of the conic section identified in the present second-order Boltzmann–Curtiss-based constitutive model has been echoed in other branches of science: notably, in the elliptic, parabolic, and hyperbolic orbits of planets and comets in the Solar System governed by Kepler's laws and Dirac cones found in some electronic band structures that describe the unusual electron transport properties of two-dimensional materials.

The second-order Boltzmann–Curtiss-based constitutive model was also investigated in the topology of the relationship between unknown viscous stresses and heat flux, and the known driving (stress and thermal) forces. In the case of velocity shear, the second-order constitutive model exhibited shear-thinning characteristics, yielding smaller shear stress compared to the first-order constitutive model. It also showed a completely different behavior for normal stress, producing non-zero normal stress for a velocity gradient in a shear flow. For compression and expansion, the topology of the second-order constitutive model became highly nonlinear and was strongly coupled to stress and thermal components for all cases. The ultimate origin of the nonlinear behavior was traced to the second-order kinematic coupling term and the hyperbolic sine nonlinear dissipative term in the second-order Boltzmann–Curtiss-based constitutive model.

Finally, in order to investigate the connection between the topology and actual flow solutions, two representative flow problems were investigated: a velocity-shear dominated force-driven Poiseuille gas flow and the compression dominated inner structure of shock waves. Trajectories of the solutions of those representative flow problems were then plotted on the topology—consisting of various conic sections and hyperbolic sine dominated surfaces—of the second-order constitutive model, demonstrating the indispensable role of the topology of the constitutive model in fluid dynamics going beyond the conventional first-order framework.

This study focused on a theoretical investigation of the existence and structure of topology in the second-order Boltzmann–Curtiss-based constitutive model for monatomic, diatomic, and polyatomic gases. However, it will be very instructive to extract information from experimental data based on the topologies identified in this study. In addition, since complex fluids such as viscoelastic fluids and soft matter must be governed by proper second-order constitutive models, the current methodology based on the closing-last balanced closure, the cumulant expansion, and decomposition may be extended to the study of the topology of constitutive equations of other complex fluids. We hope to report the results of studies of these problems in due course.

ACKNOWLEDGMENTS

R.S.M. acknowledges the support from the National Research Foundation of Korea funded by the Ministry of Science, ICT & Future Planning (No. NRF 2017-R1A2B2007634), South Korea.

REFERENCES

[1]H. K. Moffatt, G. Zaslavsky, P. Comte, and M. Tabor, *Topological Aspects of the Dynamics of Fluids and Plasmas* (Springer Science & Business Media, 2013).
[2]H. Von Helmholtz, "Uber integrale der hydrodynamichen gleichungen, welche der wirbelbewegung entsprechen," J. Reine Angew. Math **55**, 25–55 (1858).
[3]L. Kelvin, "On vortex atoms," Proc. R. Soc. Edinburgh **6**, 94–105 (1867).
[4]V. I. Arnold, "On the topology of three-dimensional steady flows of an ideal fluid," J. Appl. Math. Mech. **30**, 223–226 (1966).
[5]U. Dallmann, "Three-dimensional vortex structures and vorticity topology," Fluid Dyn. Res. **3**, 183 (1988).
[6]M. Brøns, "Topological fluid dynamics of interfacial flows," Phys. Fluids **6**, 2730 (1994).
[7]R. S. Myong and P. L. Roe, "Shock waves and rarefaction waves in magnetohydrodynamics. Part 1. A model system," J. Plasma Phys. **58**, 485 (1997).
[8]N. T. Ouellette and J. P. Gollub, "Dynamic topology in spatiotemporal chaos," Phys. Fluids **20**, 064104 (2008).
[9]L. Carrión, M. A. Herrada, and V. N. Shtern, "Topology changes in a water-oil swirling flow," Phys. Fluids **29**, 032109 (2017).
[10]R. L. Ricca, *An Introduction to the Geometry and Topology of Fluid Flows* (Springer Science & Business Media, 2012).
[11]S. Tardu, "On the topology of wall turbulence in physical space," Phys. Fluids **29**, 020713 (2017).
[12]X. Chu, B. Weigand, and V. Vaikuntanathan, "Flow turbulence topology in regular porous media: From macroscopic to microscopic scale with direct numerical simulation," Phys. Fluids **30**, 065102 (2018).
[13]F. Zafar and M. Alam, "A low Reynolds number flow and heat transfer topology of a cylinder in a wake," Phys. Fluids **30**, 083603 (2018).
[14]M. Lappa, "On the formation and morphology of coherent particulate structures in non-isothermal enclosures subjected to rotating g-jitters," Phys. Fluids **31**, 073303 (2019).
[15]P. S. Contreras, I. Ataei-Dadavi, M. F. M. Speetjens, C. R. Kleijn, M. J. Tummers, and H. J. H. Clercx, "Topological equivalence between two classes of three-dimensional steady cavity flows: A numerical-experimental analysis," Phys. Fluids **31**, 123601 (2019).
[16]K. Shariff, A. Leonard, and J. H. Ferziger, "Dynamical systems analysis of fluid transport in time-periodic vortex ring flows," Phys. Fluids **18**, 047104 (2006).
[17]X. G. Wen, "Topological orders in rigid states," Int. J. Mod. Phys. B **4**(2), 239 (1990).
[18]C. L. M. H. Navier, "Memoire sur les lois du mouvement des fluides," Mem. Acad. Sci. Inst. France **6**, 389 (1822).
[19]R. S. Myong, "Thermodynamically consistent hydrodynamic computational models for high-Knudsen-number gas flows," Phys. Fluids **11**, 2788 (1999).
[20]R. S. Myong, "A computational method for Eu's generalized hydrodynamic equations of rarefied and microscale gasdynamics," J. Comput. Phys. **168**, 47 (2001).
[21]R. S. Myong, "A generalized hydrodynamic computational model for rarefied and microscale diatomic gas flows," J. Comput. Phys. **195**, 655 (2004).
[22]Z. Jiang, W. Zhao, Z. Yuan, W. Chen, and R. S. Myong, "Computation of hypersonic flows over flying configurations using a nonlinear constitutive model," AIAA J. **57**(12), 5252 (2019).
[23]J. G. Kim and G. Park, "Thermochemical non-equilibrium parameter modification of oxygen for a two-temperature model," Phys. Fluids **30**, 016101 (2018).
[24]R. S. Myong, A. Karchani, and O. Ejtehadi, "A review and perspective on a convergence analysis of the direct simulation Monte Carlo and solution verification," Phys. Fluids **31**, 066101 (2019).
[25]T. K. Mankodi and R. S. Myong, "Quasi-classical trajectory-based non-equilibrium chemical reaction models for hypersonic air flows," Phys. Fluids **31**, 106102 (2019).
[26]T. K. Mankodi and R. S. Myong, "Erratum: Quasi-classical trajectory-based non-equilibrium chemical reaction models for hypersonic air flows [Phys. Fluids 31, 106102 (2019)]," Phys. Fluids **32**, 019901 (2020).

[27]J. H. Chae, T. K. Mankodi, S. M. Choi, and R. S. Myong, "Combined effects of thermal non-equilibrium and chemical reactions on hypersonic air flows around an orbital reentry vehicle," Int. J. Aeronaut. Space Sci. (2019).
[28]L. V. Ballestra and R. Sacco, "Numerical problems in semiconductor simulation using the hydrodynamic model: A second-order finite difference scheme," J. Comput. Phys. **195**, 320 (2004).
[29]S. K. Blau, "Conduction electrons flow like honey," Phys. Today **70**(11), 22 (2017).
[30]R. Evans, D. Frenkel, and M. Dijkstra, "From simple liquids to colloids and soft matter," Phys. Today **72**(2), 38 (2019).
[31]N. Cagney and S. Balabani, "Taylor-Couette flow of shear-thinning fluids," Phys. Fluids **31**, 053102 (2019).
[32]J. D. Evans, J. A. Cuminato, I. L. Palhares, Jr., and C. M. Oishi, "Numerical study of the stress singularity in stick-slip flow of the Phan-Thien Tanner and Giesekus fluids," Phys. Fluids **31**, 093101 (2019).
[33]J. E. Avron, "Odd viscosity," J. Stat. Phys. **92**(3–4), 543 (1998).
[34]D. Banerjee, A. Souslov, A. G. Abanov, and V. Vitelli, "Odd viscosity in chiral active fluids," Nat. Commun. **8**, 1573 (2017).
[35]S. Grozdanov and N. Kaplis, "Constructing higher-order hydrodynamics: The third order," Phys. Rev. D **93**, 066012 (2016).
[36]B. C. Eu, *Kinetic Theory of Nonequilibrium Ensembles, Irreversible Thermodynamics, and Generalized Hydrodynamics*, Relativistic Theories Vol. 2 (Springer, Switzerland, 2016).
[37]G. G. Stokes, "On the theories of the internal friction of fluids in motion, and of the equilibrium and motion of elastic fluids," Trans. Cambridge Philos. Soc. **8**, 287–305 (1845).
[38]G. Emanuel, "Bulk viscosity of a dilute polyatomic gas," Phys. Fluids A **2**, 2252–2254 (1990).
[39]G. Emanuel, "Bulk viscosity in the Navier-Stokes equations," Int. J. Eng. Sci. **36**, 1313 (1998).
[40]N. Carlevaro and G. Montani, "Bulk viscosity effects on the early universe stability," Mod. Phys. Lett. A **20**, 1729 (2005).
[41]J. F. Brady, A. S. Khair, and M. Swaroop, "On the bulk viscosity of suspensions," J. Fluid Mech. **554**, 109 (2006).
[42]F. Bahmani and M. Cramer, "Suppression of shock-induced separation in fluids having large bulk viscosities," J. Fluid Mech. **756**, R2 (2014).
[43]Y. Zhu, C. Zhang, X. Chen, H. Yuan, J. Wu, S. Chen, C. Lee, and M. Gad-el-Hak, "Transition in hypersonic boundary layers: Role of dilatational waves," AIAA J. **54**, 3039 (2016).
[44]T. K. Sengupta, A. Sengupta, N. Sharma, S. Sengupta, A. Bhole, and K. Shruti, "Roles of bulk viscosity on Rayleigh-Taylor instability: Non-equilibrium thermodynamics due to spatio-temporal pressure fronts," Phys. Fluids **28**, 094102 (2016).
[45]S. Pan and E. Johnsen, "The role of bulk viscosity on the decay of compressible, homogeneous, isotropic turbulence," J. Fluid Mech. **833**, 717 (2017).
[46]S. Singh, A. Karchani, and R. S. Myong, "Non-equilibrium effects of diatomic and polyatomic gases on the shock-vortex interaction based on the second-order constitutive model of the Boltzmann-Curtiss equation," Phys. Fluids **30**, 016109 (2018).
[47]F. Jaeger, O. K. Matar, and E. A. Müller, "Bulk viscosity of molecular fluids," J. Chem. Phys. **148**, 174504 (2018).
[48]S. Chen, X. Wang, J. Wang, M. Wan, H. Li, and S. Chen, "Effects of bulk viscosity on compressible homogeneous turbulence," Phys. Fluids **31**, 085115 (2019).
[49]S. Bhola and T. K. Sengupta, "Roles of bulk viscosity on transonic shock-wave/boundary layer interaction," Phys. Fluids **31**, 096101 (2019).
[50]R. S. Myong, "A full analytical solution for the force-driven compressible Poiseuille gas flow based on a nonlinear coupled constitutive relation," Phys. Fluids **23**, 012002 (2011).
[51]K. Xu and L. Tang, "Nonequilibrium Bhatnagar–Gross–Krook model for nitrogen shock structure," Phys. Fluids **16**, 3824 (2004).
[52]T. Morse, "Kinetic model for gases with internal degrees of freedom," Phys. Fluids **7**, 159 (1964).
[53]C. W. Chang and G. E. Uhlenbeck, "Transport Phenomena in Polyatomic Gases," Report No. CM-681, University of Michigan Engineering Research Institute, 1951.
[54]M. H. Gorji and P. Jenny, "A Fokker–Planck based kinetic model for diatomic rarefied gas flows," Phys. Fluids **25**, 062002 (2013).
[55]V. Rykov, V. Titarev, and E. Shakhov, "Shock wave structure in a diatomic gas based on a kinetic model," Fluid Dyn. **43**, 316 (2008).
[56]L. Wu, C. White, T. J. Scanlon, J. M. Reese, and Y. Zhang, "A kinetic model of the Boltzmann equation for non-vibrating polyatomic gases," J. Fluid Mech. **763**, 24 (2015).
[57]C. Curtiss, "The classical Boltzmann equation of a gas of diatomic molecules," J. Chem. Phys. **75**, 376 (1981).
[58]C. Curtiss, "The classical Boltzmann equation of a molecular gas," J. Chem. Phys. **97**, 1416 (1992).
[59]B. C. Eu, *Kinetic Theory and Irreversible Thermodynamics* (Wiley, New York, 1992).
[60]B. C. Eu and Y. G. Ohr, "Generalized hydrodynamics, bulk viscosity, and sound wave absorption and dispersion in dilute rigid molecular gases," Phys. Fluids **13**, 744 (2001).
[61]R. S. Myong, "On the high Mach number shock structure singularity caused by overreach of Maxwellian molecules," Phys. Fluids **26**, 056102 (2014).
[62]A. Rana, R. Ravichandran, J. H. Park, and R. S. Myong, "Microscopic molecular dynamics characterization of the second-order non-Navier-Fourier constitutive laws in the Poiseuille gas flow," Phys. Fluids **28**, 082003 (2016).
[63]S. Chapman and T. G. Cowling, *The Mathematical Theory of Non-uniform Gases* (Cambridge University Press, Cambridge, 1970).
[64]M. S. Cramer, "Numerical estimates for the bulk viscosity of ideal gases," Phys. Fluids **24**, 066102 (2012).
[65]L. Onsager, "Reciprocal relations in irreversible processes. I," Phys. Rev. **37**(4), 405 (1931).
[66]D. A. Brannan, M. F. Esplen, and J. J. Gray, *Geometry* (Cambridge University Press, 1999).
[67]R. E. Khayat and B. C. Eu, "Generalized hydrodynamics, normal-stress effects, and velocity slips in the cylindrical Couette flow of Lennard-Jones fluids," Phys. Rev. A **39**(2), 728 (1989).
[68]R. S. Myong, "A computationally efficient framework for modeling microscale and rarefied gas flows based on new constitutive relations," AIAA Paper 2010-563, 2010.
[69]R. Fitzpatrick, *Classical Mechanics—An Introductory Course* (The University of Texas at Austin, 2006).
[70]J.-N. Fuchs, L.-K. Lim, and G. Montambaux, "Interband tunneling near the merging transition of Dirac cones," Phys. Rev. A **86**, 063613 (2012).
[71]A. Grüneis, C. Attaccalite, A. Rubio, D. V. Vyalikh, S. L. Molodtsov, J. Fink, R. Follath, W. Eberhardt, B. Büchner, and T. Pichler, "Angle-resolved photoemission study of the graphite intercalation compound KC8: A key to graphene," Phys. Rev. B **80**(7), 075431 (2009).
[72]R. S. Myong, "Analytical solutions of shock structure thickness and asymmetry in Navier–Stokes/Fourier framework," AIAA J. **52**(5), 1075 (2014).
[73]H. Grad, "The profile of a steady plane shock wave," Commun. Pure Appl. Math. **5**, 257 (1952).
[74]M. Al-Ghoul and B. C. Eu, "Generalized hydrodynamics and shock waves," Phys. Rev. E **56**, 2981 (1997).
[75]M. Al-Ghoul and B. C. Eu, "Generalized hydrodynamic theory of shock waves in rigid diatomic gases," Phys. Rev. E **64**, 046303 (2001).
[76]H. M. Mott-Smith, "The solution of the Boltzmann equation for a shock wave," Phys. Rev. **82**, 885 (1951).
[77]Z. Jiang, W. Zhao, W. Chen, and R. K. Agarwal, "Computation of shock wave structure using a simpler set of generalized hydrodynamic equations based on nonlinear coupled constitutive relations," Shock Waves **29**, 1227 (2019).
[78]E. Josyula, P. Vedula, and W. F. Bailey, "Kinetic solution of shock structure in a non-reactive gas mixture," AIAA Paper 2010-817, 2010.
[79]N. T. Le, H. Xiao, and R. S. Myong, "A triangular discontinuous Galerkin method for non-Newtonian implicit constitutive models of rarefied and microscale gases," J. Comput. Phys. **273**, 160 (2014).

[80]L. P. Raj, S. Singh, A. Karchani, and R. S. Myong, "A super-parallel mixed explicit discontinuous Galerkin method for the second-order Boltzmann-based constitutive models of rarefied and microscale gases," Comput. Fluids **157**, 146 (2017).
[81]F. Bassi and S. Rebay, "A high-order accurate discontinuous finite element method for the numerical solution of the compressible Navier–Stokes equations," J. Comput. Phys. **131**, 267 (1997).
[82]J. Qiu and C. W. Shu, "Hermite WENO schemes and their application as limiters for Runge–Kutta discontinuous Galerkin method: One-dimensional case," J. Comput. Phys. **193**, 115 (2004).
[83]H. Alsmeyer, "Density profiles in argon and nitrogen shock waves measured by the absorption of an electron beam," J. Fluid Mech. **74**, 497 (1976).
[84]M. Camac, "Argon shock structure," in *Proceedings of the Fourth International Symposium on Rarefied Gas Dynamics* [Adv. Appl. Mech. **1**, 240 (1965)].
[85]W. Garen, R. Synofzik, and A. Frohn, "Shock tube for generating weak shock waves," AIAA J. **12**, 1132 (1974).
[86]M. Linzer and D. Hornig, "Structure of shock fronts in argon and nitrogen," Phys. Fluids **6**, 1661 (1963).
[87]M. Fogiel, *Handbook of Mathematical, Scientific, and Engineering: Formulas, Tables, Functions, Graphs, Transforms* (Research and Education Assoc., 1997).